

LUT UNIVERSITY
LUT School of Energy Systems
LUT Mechanical Engineering

Markus Kastinen

**ROLLING-ELEMENT BEARING STIFFNESS ESTIMATION FROM RELATIVE
SHAFT DISPLACEMENT**

Examiners: Prof. Jussi Sopenen
D.Sc. (Tech.) Emil Kurvinen
Supervisor: D.Sc. (Tech.) Timo Holopainen

TIIVISTELMÄ

LUT-Yliopisto
LUT School of Energy Systems
LUT Kone

Markus Kastinen

Vierintälaakerin jäykkyyden määrittäminen akselin suhteellisesta poikkeamasta

Diplomityö

2019

68 sivua, 42 kuvaa, 13 taulukkoa ja 4 liitettä

Tarkastajat: Prof. Jussi Sopenen
Tkt Emil Kurvinen

Hakusanat: induktiomoottori, kapasitiivinen anturi, laakerijäykkyys, urakuulalaakeri, vierintälaakeri

Sähkömoottorin dynamiikan arvioimiseksi vaaditaan tarkka tieto laakereiden jäykkyyksistä. Laakerin jäykkyydellä on vaikutus sähkömoottorin runkoon siirtyviin värähtelyihin sekä laakerijäykkyys voi vaikuttaa sähkömoottorin kriittisiin nopeuksiin. Vierintälaakerin jäykkyydsmatriisi on usein saatavilla laakerivalmistajalta. Yleensä laakerivalmistajan ilmoittama jäykkyydsmatriisi ottaa huomioon vain vierintäelimien sekä ulko- ja sisäkehien välisien kontaktien jäykkyyden jättäen huomioimatta laakerin ulkokehän sekä laakeripesän sisähalkaisijan väläksen. Tämä laakerin ja laakeripesän välinen väläys aiheuttaa jäykkyyden alenemisen ulkokehän elastisen muodonmuutoksen vuoksi.

Tässä diplomityössä tarkastellaan 11 kW induktiomoottorin urakuulalaakereiden jäykkyyttä kokeellisesti käyttämällä 0,16 μm resoluutiolla toimivaa kapasitiivista paikka-anturia. Kokeellinen menetelmä laakerijäykkyyden määrittämiseksi perustuu roottorilla sijaitsevan massaepätasapainon aiheuttamaan voimaan sekä mitattuun roottorin suhteelliseen siirtymään. Laakerijäykkyyttä tutkitaan kolmella eri laakerin aksiaalisella esikiristyksellä ja tuloksia verrataan numeerisiin sekä analyttisiin menetelmin laskettuihin laakerijäykkyyksiin. Numeerisissa menetelmissä käytettävät ohjelmistot ovat BearinX sekä MATLAB RoBeDyn-laskentaohjelmalla.

Kokeellisesti määritetyt jäykkyydet olivat 62 % – 85 % pienempiä kuin numeerisesti määritetyt jäykkyydet. Ero tuloksien välillä johtuu mahdollisesti numeeristen mallien laakereiden reunaehdoista, joissa laakerin ulkokehän siirtymät estettiin, sekä mittausvirheistä. Kokeellisessa menetelmässä oli mahdollista nähdä laakerin esikiristyksen vaikutus laakerin jäykkyyteen.

ABSTRACT

LUT University
LUT School of Energy Systems
LUT Mechanical Engineering

Markus Kastinen

Rolling-element bearing stiffness estimation from relative shaft displacement

Master's thesis

2019

68 pages, 42 figures, 13 tables and 4 appendices

Examiners: Prof. Jussi Sopenen
D.Sc. (Tech.) Emil Kurvinen

Keywords: bearing stiffness, capacitive sensor, deep-groove ball bearing, induction motor, rolling-element bearing

To analyze the dynamic behavior of an electric motor an accurate description of the bearing stiffness is required. Stiffness of the bearings will have an effect to the vibrations transferred to the motor frame and can have an effect to the critical speeds of the system. Stiffness matrix of the bearing is usually provided by the bearing manufacturer and usually takes only in account the contact stiffness between the rolling-elements and races. Thus, effect of clearance between the bearing outer race and bearing housing are not taken into account which have been proven to lower the stiffness due to elastic deformation of the outer race.

In this thesis, the stiffness of deep-groove ball bearings used in a 11 kW induction motor is estimated experimentally by using a capacitive displacement sensor with 0,16 μm resolution. Experimental method is based on different static unbalance cases of the rotor to calculate the stiffness from a relative displacement caused by a known rotating radial force. Stiffnesses are acquired experimentally with three different axial preloads of the bearing and the results are compared to numerically and analytically acquired bearing stiffnesses. Numerical methods include the computational tools that are BearinX-software and RoBeDyn-toolbox for MATLAB.

Experimentally acquired stiffnesses are 62 % to 85 % lower than with numerical methods. Reason for the large difference is possibly due to the boundary conditions used in the computational models, which assume the outer race to be fixed, and measurement errors. With the experimental method, the effect of bearing preload to the stiffness of the bearing was possible to detect.

ACKNOWLEDGEMENTS

I would like to thank Prof. Jussi Sopanen and D.Sc. (Tech.) Emil Kurvinen for their guidance and enthusiasm toward my thesis. Also, thanks to the team of Laboratory of Machine Dynamics for their help with the experimental measurements.

From ABB, I would like to thank D.Sc. (Tech.) Timo Holopainen for supervising this thesis, M.Sc. (Tech.) Olli Liukkonen and D.Sc. (Tech.) Markku Niemelä for their advices during my thesis and M.Sc. (Tech.) Iiro Pelli with his help with the experimental measurements.

Lastly, I would like to thank my family and friends for their support during my studies.



Markus Kastinen

Lappeenranta 11.6.2019

TABLE OF CONTENTS

TIIVISTELMÄ

ABSTRACT

ACKNOWLEDGEMENTS

TABLE OF CONTENTS

LIST OF SYMBOLS AND ABBREVIATIONS

1	INTRODUCTION	10
1.1	Bearing stiffness	11
1.2	Motivation and research problem	11
1.3	Research methods	12
2	BEARING STIFFNESS AND EXISTING METHODS FOR STIFFNESS ESTIMATION	13
2.1	Ball bearings	13
2.2	Bearing stiffness	16
2.3	Estimation of bearing stiffness	20
2.3.1	Analytical and numerical methods	20
2.3.2	Experimental methods	26
2.3.3	Main findings from the literature review	28
3	METHODS USED FOR BALL BEARING STIFFNESS EVALUATION.....	29
3.1	Software	29
3.2	Deep-groove ball bearing geometry measurements.....	29
3.3	Test rig and measurement setups	32
3.3.1	Geometrical measurements.....	33
3.3.2	Modal analysis of the rotor	34
3.3.3	Measurement procedure of shaft displacement measurements.....	36
3.3.4	Post-processing	39
4	ANALYTICAL, NUMERICAL AND EXPERIMENTAL RESULTS OF DEEP-GROOVE BALL BEARING STIFFNESS ESTIMATION.....	43
4.1	Numerical and analytical results.....	43
4.2	Shaft displacement measurements	44
4.2.1	Non-Drive End.....	45

4.2.2	Drive-End.....	48
4.3	Estimation of bearing stiffness	50
4.4	Comparison of experimental method to numerical and analytical methods.....	53
5	DISCUSSION.....	57
5.1	Error sources	59
5.2	Future research.....	60
6	CONCLUSIONS.....	62
7	REFERENCES.....	64

APPENDICES

Appendix I: Bearing dimensions and bearing housing bore surface roughnesses

Appendix II: Modal analysis results

Appendix III: Rotor-hub assembly drawing

Appendix IV: 1X-components of shaft displacement measurements

LIST OF SYMBOLS AND ABBREVIATIONS

B	Bearing width [mm]
c_{dy}	Radial clearance [mm]
d	Inner diameter of inner race [mm]
D	Outer diameter of outer race [mm]
D_b	Ball diameter [mm]
\mathbf{e}	Relative displacement vector
e	Eccentricity [m]
e_x, e_y, e_z	Relative displacement between rings [m]
E'	Effective modulus of elasticity [N/m ²]
E_a	Elastic modulus of ball [N/m ²]
E_b	Elastic modulus of race [N/m ²]
f	Elliptical integral of first kind
f_s	Sampling rate [1/s]
\mathbf{F}	Vector of applied loads and moments
F_a	Applied external axial load [N]
F_i	Load [N]
F_r	Applied external radial load [N]
$F_{unbalance}$	Unbalance force [N]
g	Preload [m]
\mathbf{K}_T	Tangent stiffness matrix
k_{ij}	Stiffness [N/m]
K	Load-deflection constant [N/m ^{1.5}]
\bar{K}	Average oscillation factor
K_{axial}	Stiffness in axial direction [N/m]
K_i	Load-deflection constant of ball-inner race contact [N/m ^{1.5}]
K_o	Load-deflection constant of ball-outer race contact [N/m ^{1.5}]
K_{pc}	Geometrical factor for point contact [N/m ^{1.5}]
K_{radial}	Stiffness in radial direction [N/m]
m	Unbalance mass [kg]

n	Iteration step
N	Number of samples
P	Load on rolling-element [N]
\mathbf{q}	Displacement vector
\mathbf{q}_1	Displacement vector of unbalance mass 1
\mathbf{q}_2	Displacement vector of unbalance mass 2
\mathbf{dq}	Displacement difference vector
\mathbf{Q}_b	Bearing force vector
\mathbf{Q}_{ext}	External force vector
q_j	Displacement [m]
r_b	Ball radius [m]
r_c	Correlation coefficient
r_{in}	Inner groove radius [mm]
r_{out}	Outer groove radius [mm]
R	Curvature sum [m]
R_{in}	Inner raceway radius [m]
x, y, z	Displacements in Cartesian coordinates [m]
Z	Number of rolling-elements
α	Contact angle [rad]
β	Azimuth angle [rad]
δ	Deflection [m]
δ_r	Radial deflection [m]
δ_a	Axial deflection [m]
δ_x	Displacement of inner race in direction of radial load [m]
δ_y	Displacement of inner race in direction perpendicular to radial load [m]
Δf	Resolution of Fast Fourier Transform [1/s]
ε	Elliptical integral of second kind
η_i	Angle between the direction of the inner race and the radius through the centerline of i th rolling-element [°]
$\theta_x, \theta_y, \theta_z$	Rotations in Cartesian coordinates [°]
κ	Ellipticity parameter

ν_a	Poisson's ratio of the ball
ν_b	Poisson's ratio of the race
φ	Rotation angle of the cage [°]
ϕ	Contact angle of the ball [rad]
ω	Rotation speed [rad/s]
AC	Alternative Current
ACBB	Angular Contact Ball Bearing
DC	Direct Current
DE	Drive End
DGBB	Deep-Groove Ball Bearing
DOF	Degrees of Freedom
EDMS	Electric Motor-Driven System
FE	Finite Element
LUT	Lappeenranta-Lahti University of Technology
MRO	Mechanical Run-Out
NDE	Non-Drive End
ODS	Operational Deflection Shape
PLC	Programmable Logic Controller
RMS	Root Mean Square
RoBeDyn	Rotor-Bearing Dynamics-toolbox
RPM	Revolutions per Minute
VFC	Variable Frequency Converter
1X	Once per revolution excitation
2X	Twice per revolution excitation

1 INTRODUCTION

Electric motors are used to convert electrical power to mechanical power in a wide area of applications ranging from small commercial applications to large industrial machinery. It is estimated that 43 % to 46 % of all global energy consumption is used by electric motor – driven systems (Waide & Brunner 2011, p. 11). Electric motors can be divided into two groups based on the type of the current source: to direct current (DC) or alternative current (AC) motors. Main components in every electric motor are the stator and rotor supported by bearings in both ends. Figure 1 presents an exploded view of a 3-phase induction motor.

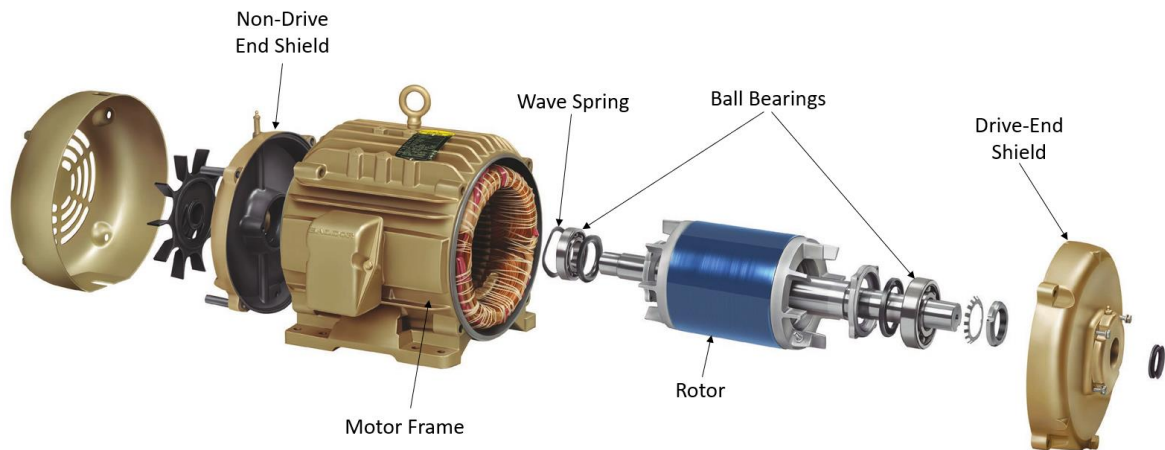


Figure 1. Exploded view of a 3-phase induction motor (Mod. ABB 2014).

Bearings are needed to connect the rotating rotor to the stationary motor frame to allow it to rotate with a minimal friction. Minimizing the friction reduces the power losses in the electric motor. Bearing types that are commonly used in electric motors are rolling-element bearings and hydrodynamic bearings. The used bearing type is chosen based on the requirements that the application defines, these requirements typically are the loads that arises during the operation and the direction of loads, rotation speed and required bearing life. Rolling-element bearings are the most commonly used bearing type in electric motors. While those are not the only type of bearings that can be used, rolling-element bearings are chosen in many applications due to the price, availability and load capacity. (Herbert 2011, p. 189.)

Rolling-element bearings are prone to fail due to different tribological phenomena affecting to them, such as abrasive and fatigue wear. It is estimated that 51 % of all electric motor failures are caused by the bearings which can fail due to e.g. lubrication error, shaft overload or vibrations. (ABB 2015, p 2.) Besides tribological phenomena, installation error of the bearings can lead to an early failure of the electric motor.

1.1 Bearing stiffness

Bearing stiffness is required information for designers since it affects to the dynamic behavior of the system. Stiffness along with damping of the bearings determines the transfer of vibrations from rotor to the bearing housing. Bearings have also an effect to the critical speeds of the rotor which can be studied with a critical speed map that presents the critical speeds of the rotor as a function of bearing stiffness. With rigid rotors the critical speeds are determined by bearing stiffness and rotor inertia while critical speeds of flexible rotors are determined also by rotor stiffness and mass distribution (Gargiulo 1980, p. 109). An example of a critical speed map with a simple shaft is presented in Figure 2.

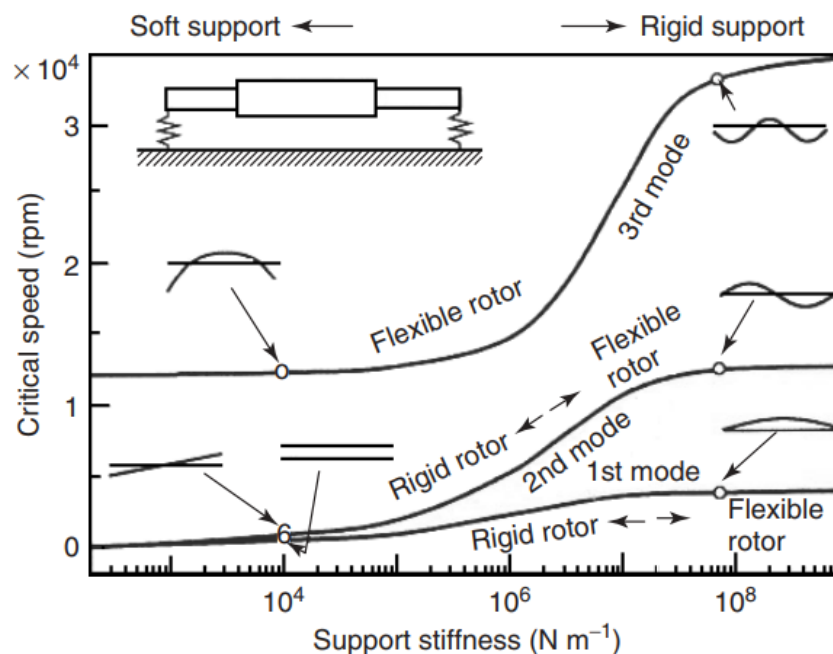


Figure 2. Critical speed map with rotor modeshapes (Ishida & Yamamoto 2012, p. 2).

1.2 Motivation and research problem

The values for bearing stiffness are typically given by bearing manufacturer, when the used bearing type, the loading condition and rotation speeds are provided. However, these values

might not be accurate enough for example due to the different boundary conditions of the supporting structure and different loads experienced by the actual machine that it is designed for. Study by Bauer & Werner (2016) concluded that the given stiffness values by supplier were 46 % higher than the actual bearing stiffness in a 650 kW induction motor. Stiffnesses were estimated by measuring the critical speeds of the motor with accelerometers and matching the stiffnesses of the bearings in a computer model of the rotor to achieve the same critical speeds. (Bauer & Werner 2016, p. 1 – 9.)

The bearing stiffness is a required information to analyze the dynamics of the system. With small and medium sized motors where rotors can be assumed to be rigid, the stiffness of the bearings are crucial to know to estimate the critical speeds of the motor to avoid excess vibrations that could damage the motor. With large sized motors, where rotors can be assumed to be flexible, the stiffness of the bearings is one contributing factor on the dynamics of the motor.

Estimation of bearing stiffness has been under study in industry and research community, and it has been developed numerous analytical, numerical and experimental methods to estimate the stiffness. Experimental methods to estimate the bearing stiffness has been limited mainly to test rigs that are specifically designed to study the stiffness, not from the actual system.

In this thesis, the stiffness of rolling-element bearings, used in a medium sized electric motor, is studied from experimentally acquired shaft displacement data measured with a capacitive displacement sensor. Research problem in this thesis is how bearing stiffness can be estimated experimentally from shaft displacement data of an electric motor.

1.3 Research methods

In Chapter 2, stiffness of a rolling-element bearing is discussed by presenting the parameters that have an effect on it. Literature research is also used to present the tools that have been developed or are currently in use to determine the bearing stiffness. Literature review is conducted mainly by using the databases of LUT-Finna, Scopus and Google Scholar. In Chapter 3, an experimental method to estimate the bearing stiffness is presented including the used instruments and the measurement procedure.

2 BEARING STIFFNESS AND EXISTING METHODS FOR STIFFNESS ESTIMATION

This chapter presents the key findings from the literature presenting the multiple parameters affecting to the rolling-element bearing stiffness and proposed methods to evaluate the bearing stiffness.

2.1 Ball bearings

In ball bearings the load is carried by ball shaped rolling-elements and is used in applications to support mainly radial loads but can also tolerate axial loads. Multiple different designs of ball bearing exist, some of which are more suitable for higher speeds, tolerate higher axial loads and misalignments than the others. The two main ball bearing types are deep-groove ball bearings (DGBBs) and angular contact ball bearings (ACCBs). Main components in ball bearings are the outer and inner race, balls and a cage that keeps the distance between the balls constant. In DGBB the contact angle between the ball and inner and outer races is close to zero without an axial load whereas in ACCB there is a contact angle present. Figure 3 presents an illustration of a DGBB.

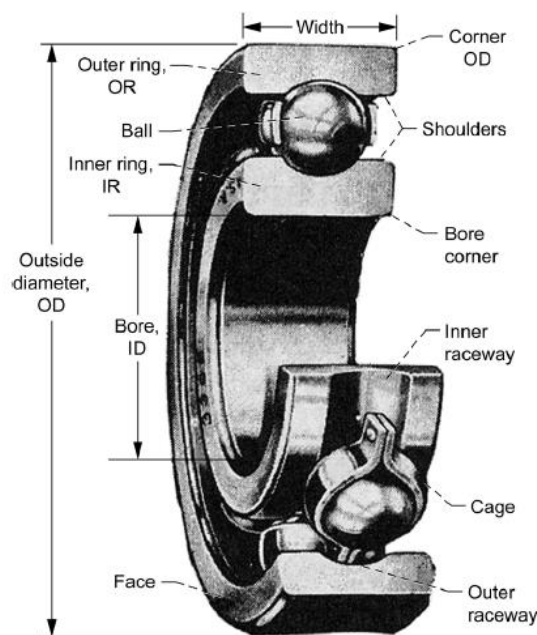


Figure 3. Deep-groove ball bearing (Mod. Zaretsky 2013, p. 11).

The load-displacement curve of ball bearings is non-linear, which is also the case with every rolling-element bearings. In DGBBs, the contact between a single ball shaped rolling-element and inner and outer races is a point contact. Under a radial load, the area of contact will increase and will have an elliptical shape. Shape of the contact area is different for different rolling-element bearings, e.g. in roller bearings the area of contact prior to applied load is a line contact and after the applied load the area of contact is increased as a rectangular shape. Figure 4 presents the elliptical contact areas of a DGBB. (Hamrock & Anderson 1983, p. 10 & 17.)

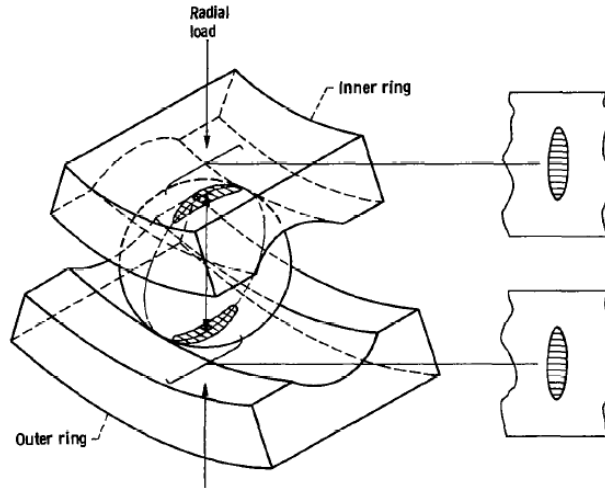


Figure 4. Elliptical contact areas of DGBB under a radial load (Hamrock & Anderson 1983, p. 18).

The load-deflection relationship for a single ball and the races in a ball bearing is expressed by Equation (1) (Hamrock & Anderson 1983, p. 20).

$$P = K\delta^{3/2} \quad (1)$$

Where δ is the deflection (m) caused by the load on the rolling-element P (N). In Equation (1), K is the load-deflection constant ($\text{N}/\text{m}^{1.5}$) and for a ball bearing it is expressed by Equation (2) (Hamrock & Anderson 1983, p. 20).

$$K = \frac{1}{\left[\left(\frac{1}{K_i} \right)^{2/3} + \left(\frac{1}{K_o} \right)^{2/3} \right]^{3/2}} \quad (2)$$

Where K_i is the load-deflection constant of the inner race and the ball ($\text{N/m}^{1.5}$) and K_o is the load-deflection constant of the outer race and the ball ($\text{N/m}^{1.5}$). Load-deflection constants K_i and K_o are expressed by Equation (3) (Hamrock & Anderson 1983, p. 20).

$$K_{i,o} = \pi \kappa E' \sqrt{\frac{2\varepsilon R}{9f^3}} \quad (3)$$

Where κ is ellipticity parameter that is dependent on the radius of curvature ratio, E' is effective modulus of elasticity (N/m^2), R is curvature sum (m) and f and ε are elliptic integrals of first and second kind, respectively (Hamrock & Anderson 1983, p. 20.) Values for κ are from 1 to 18.1871, f from 1.5708 to 4.2895 and for ε 1.5708 to 1.0057 (Hamrock & Anderson 1983, p. 52). E' is calculated from Equation (4) (Hamrock & Anderson 1983, p. 19).

$$E' = \frac{2}{\frac{1-\nu_a^2}{E_a} + \frac{1-\nu_b^2}{E_b}} \quad (4)$$

Where ν is the Poisson's ratio and E is the modulus of elasticity (N/m^2). Subscript a indicates ball and subscript b race (Hamrock & Anderson 1983, p. 29). The total stiffness of the bearing is then calculated as a sum of each contacts. Difficulties in estimation of the bearing stiffness are that due to clearances in the bearing, not every rolling-elements are loaded evenly some of which are not loaded at all. Figure 5 presents radial clearances of a DGBB without an applied radial load (a), with an applied radial load without an elastic deformation (b) and with an applied radial load with an elastic deformation (c).

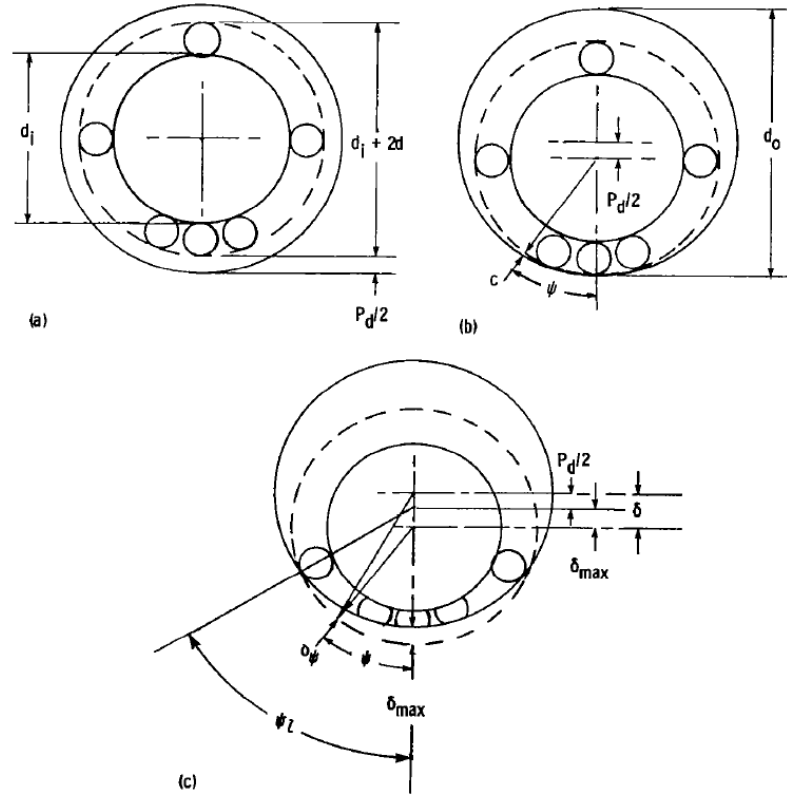


Figure 5. DGBB clearances under radial load (Hamrock & Anderson 1983, p. 21).

2.2 Bearing stiffness

The rolling-element bearing can be considered to have six degrees of freedom (DOF), three translational (x, y, z) and three rotational ($\theta_x, \theta_y, \theta_z$). By expressing the relative displacement between inner and outer races of the bearing by a vector $\mathbf{q} = [x \ y \ z \ \theta_x \ \theta_y \ \theta_z]^T$ caused by an applied load and moment vector $\mathbf{F} = [F_x \ F_y \ F_z \ M_{\theta_x} \ M_{\theta_y} \ M_{\theta_z}]^T$, stiffness of the rolling-element bearing can be expressed as the first derivative of the load with respect to the displacement (Guo & Parker 2012, p. 35 – 36; Ragulskis et al. 1974, p. 49).

$$k_{ij} = \frac{\partial F_i}{\partial q_j} \quad (5)$$

Where F_i is the applied load and q_i is the displacement. Subscript i indicates the direction of load and subscript j indicates the direction of displacement, e.g. k_{xx} and k_{yy} are radial stiffnesses. Stiffness of a rolling-element bearing is then expressed as a 6x6 stiffness matrix. Stiffness matrix and the six DOFs of the bearing are presented in Figure 6. Diagonal terms

of the stiffness matrix represent radial, axial and tilting stiffnesses and off-diagonal terms are cross-coupling stiffness terms. Sixth row and column are zero due to free rotation. (Guy & Parker 2012, p. 35 – 36).

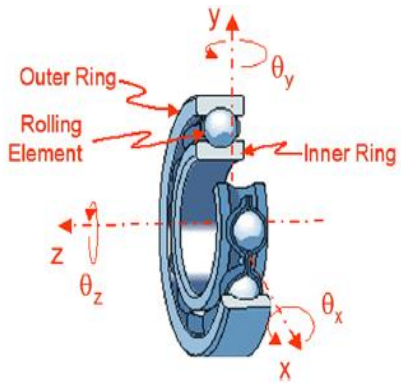
$$\begin{Bmatrix} F_x \\ F_y \\ F_z \\ M_x \\ M_y \\ M_z \end{Bmatrix} = \begin{bmatrix} k_{xx} & k_{yx} & k_{zx} & k_{\theta_x x} & k_{\theta_y x} & 0 \\ k_{xy} & k_{yy} & k_{zy} & k_{\theta_x y} & k_{\theta_y y} & 0 \\ k_{xz} & k_{yz} & k_{zz} & k_{\theta_x z} & k_{\theta_y z} & 0 \\ k_{x\theta_x} & k_{y\theta_x} & k_{z\theta_x} & k_{\theta_x \theta_x} & k_{\theta_y \theta_x} & 0 \\ k_{x\theta_y} & k_{y\theta_y} & k_{z\theta_y} & k_{\theta_x \theta_y} & k_{\theta_y \theta_y} & 0 \\ 0 & 0 & 0 & 0 & 0 & 0 \end{bmatrix} \begin{Bmatrix} \delta_x \\ \delta_y \\ \delta_z \\ \beta_x \\ \beta_y \\ \beta_z \end{Bmatrix}$$


Figure 6. 6x6 bearing stiffness matrix (highlighted with red) (Mod. Hambric et al. 2013, p. 5).

The effect of different terms is dependent on the type of rolling-element and the contact angle. In DGBBs and straight roller bearings the most dominant are the horizontal and vertical stiffness terms whereas in ACCBs and in taper roller type bearings the most dominant are the coupling terms. Figure 7 Presents the effect of contact angle to stiffness terms in radially (left) and axially (right) preloaded ball bearing. (Lim & Chen 1990, p. 189 – 193.)

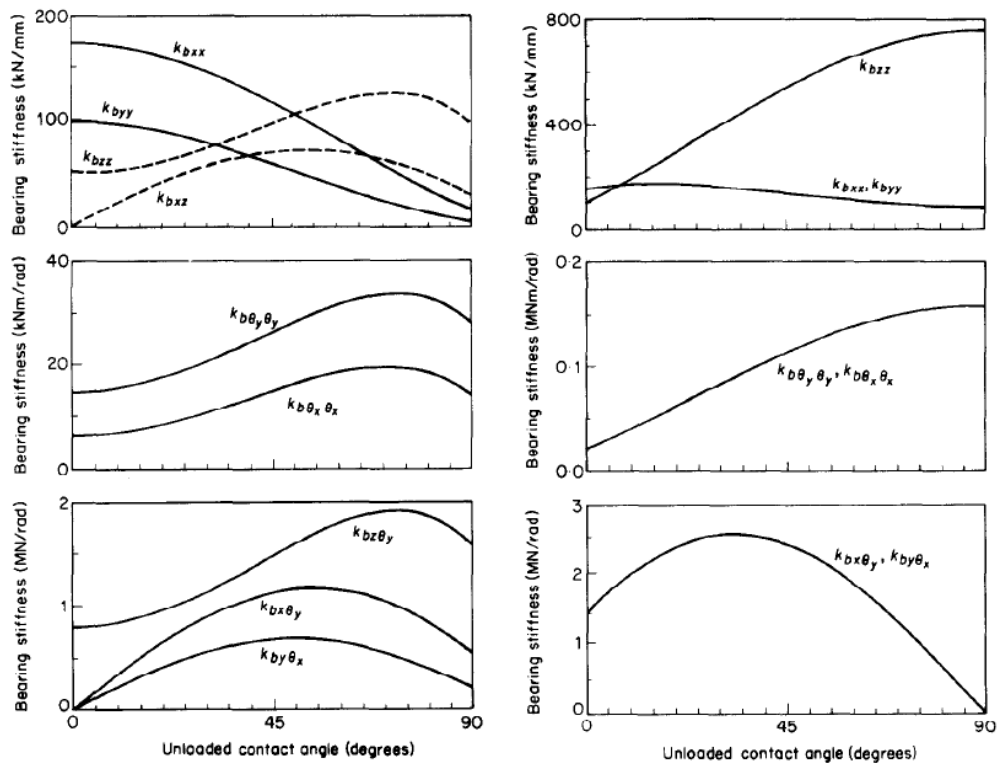


Figure 7. Stiffness coefficients of ball bearing as a function of unloaded contact angle, for a DGBB the contact angle is zero (Lim & Chen 1990, p. 191 & p. 193).

Stiffness of the rolling-element bearing depends on the type of rolling-elements, axial preload, clearance, operation speed, lubricant (Stone 1982, p. 536) and fit between the outer race of the bearing and bearing housing (Bauer & Werner 2016, p. 4.)

Preload is applied to rolling-element bearings to reduce the internal clearance, which is the distance that one bearing race can move relative to another. Reduce in internal clearance will distribute the load more evenly along the circumference of the bearing which will lead to enhanced stiffness. Besides increased stiffness, preload is applied to ensure the correct operation of the bearing without skidding. Decrease in internal clearance will reduce noise caused by the bearing while operating and it is shown that DGBBs with a slight negative clearance will have greater life factor when compared to DGBBs with a large negative clearance or positive clearance (Oswald et al. 2012, p. 11). Determination of adequate bearing preload is important since an excessive preload can shorten the lifespan of the bearing due to heat generation caused by the friction (Xiaohu et al. 2016, p. 11). Ball bearings can be preloaded axially by using spring washers, springs or shims. Effect of preload to

radial and axial stiffnesses of SKF EEB 3-2Z DGBB acquired experimentally (solid line) and numerically, with two different radial clearances of 0 mm (dotted line) and 0,01 mm (dashed line) is presented in Figure 8. Radial clearance for the experimental result is not given and clearances for numerical method are the two extremes given by manufacturer. (Guo & Parker 2012, p. 37 – 39).

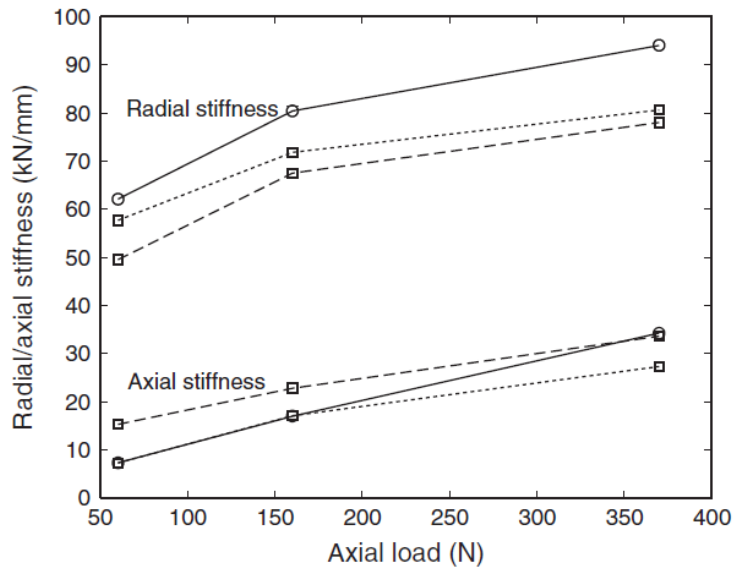


Figure 8. Radial and axial stiffness acquired numerically, with 0 mm radial clearance (dotted line) and 0,01 mm radial clearance (dashed line), and experimentally (solid line) with an unknown radial clearance (Guo & Parker 2012, p. 38).

In different rotor-bearing systems, multiple different fit types can be used. Free bearings are fixed only in radial direction to allow axial movement due to thermal expansion of the shaft and fixed bearings are fixed both in radial and axial directions. In electric motors, the drive end (DE) bearing is typically fixed and non-drive end (NDE) is free. Bearing stiffness can decrease with a loose fit, between the bearing and the housing, due to elastic deformation (Bauer & Werner 2016, p. 5).

Bearing stiffness is affected by high rotational speeds due to centrifugal and gyroscopic moments during the high-speed operation. Study by Kurvinen et al. (2015) concluded that the centrifugal force and gyroscopic moment, which will increase as the speed increases, will decrease the bearing stiffness. With low rotation speeds the bearing stiffness is nearly constant. (Kurvinen et al. 2015, p. 240 – 260.)

2.3 Estimation of bearing stiffness

In the following chapter different methods to estimate the rolling-element bearing stiffness and theoretical background behind them are discussed. Methods to estimate the stiffness include analytical, numerical and experimental methods. Bearing stiffness has been studied experimentally mostly by modal analysis and waterfall-plot analysis.

2.3.1 Analytical and numerical methods

Several analytical formulas have been introduced to estimate the bearing stiffness, these formulas are mostly based on the geometry of the ball bearing components and the affecting loads. These are fairly simple to use but the drawbacks are in the accuracy of the results due to simplifications. Analytical formulations can be roughly be divided into two categories: ones expressing the stiffness as a function of the applied load and ones expressing the stiffness as a function of the displacement.

El-Sayed (1980) derived an equation for static stiffness of DGBBs and later verified the accuracy of the equation by experimental measurements (El-Sayed 1980, p. 89 – 94). In the same year, Gargiulo (1980) presented equations to estimate the radial and axial deflections and stiffnesses for various type of rolling-element bearings, including DGBBs. Gargiulo defined radial deflection of DGBB in Equation (6) and axial deflection in Equation (7). (Gargiulo 1980, p. 108 – 109.)

$$\delta_r \approx 1,2750 \cdot 10^{-6} \cdot \sqrt[3]{\frac{F_r^2}{D_b Z^2 \cos^5 \alpha}} \quad (6)$$

$$\delta_a \approx 4,3604 \cdot 10^{-7} \cdot \sqrt[3]{\frac{F_a^2}{D_b Z^2 \sin^5 \alpha}} \quad (7)$$

Where F_r is the applied external radial force to the bearing (N), D_b is the diameter of the ball (mm), Z is the number of rolling-elements, α is the contact angle (rad) and F_a is the applied external axial force to the bearing (N). Gargiulo's radial stiffness estimation for DGBB is presented in Equation (8) and axial stiffness in Equation (9). (Gargiulo 1980 p. 108 – 109.)

$$K_{radial} \approx 1,1776 \cdot 10^6 \cdot \sqrt[3]{D_b F_r Z^2 \cos^5 \alpha} \quad (8)$$

$$K_{axial} \approx 3,4386 \cdot 10^6 \cdot \sqrt[3]{D_b F_a Z^2 \sin^5 \alpha} \quad (9)$$

Equations (6) to (9) by Gargiulo (1980) are modified to yield results in SI-units since in the original article imperial units are used, Equations (6) and (7) gives deflection in (m) and Equations (8) and (9) gives stiffness in (N/m). Equations are capable to calculate the radial and axial stiffness by assuming the outer race to be rigid. Several newer methods and tools to estimate the stiffness of the bearings are verified and compared with Gargiulo's equations. For example, in computational program Dyrobes (Dyrobes 2017).

Houpert (1997) defined equivalent linearized bearing stiffness for a point contact, Equation (10) (Houpert 1997, p. 854 – 857).

$$K_{radial} = 0.3743 \cdot (K_{pc} Z)^{2/3} \cdot (\cos \alpha)^{5/3} \cdot F_r^{1/3} \quad (10)$$

where K_{pc} is a geometrical factor for a point contact ($\text{N/m}^{1.5}$) defined by Equation (11). In Equation (11), \bar{K} is the average osculation factor. (Houpert 1997, p. 854 – 857.)

$$K_{pc} = 3.37 \cdot 10^{10} \cdot \left(\frac{1+\bar{K}}{\bar{K}}\right)^{0.345} \cdot (D_b \cdot 10^{-3})^{0.5} \quad (11)$$

Ragulskis et al. (1979) derived expression for rolling-element bearing radial stiffness in static equilibrium during rotation. By expressing the contact between the races and rolling-elements by Hertzian contact theory, restoring force to be sum of elastic forces on the loaded rolling-elements and restoring force in perpendicular to the direction of applied load to be zero, Ragulskis et al. (1979) resulted for the expression of radial stiffness as a function of preload or clearance, displacement, angle between applied load and the radius of i th rolling-element and coefficient of proportionality which depends on rolling-element design and material. Figure 9 presents a radially loaded ball bearing. (Ragulskis et al. 1979 p. 46 – 51.)

By substituting Equation (14) to Equation (12), Equation (12) can be written as:

$$P_i = K[g + \delta_x \cos(\eta_i) + \delta_y \sin(\eta_i)]^{3/2} \cos(\eta_i) \quad (15)$$

The total elastic force is the sum of the elastic forces of each rolling-element and can be written as (Ragulskis et al. 1979 p. 48).

$$P = \sum P_i = K \sum_{i=0}^{Z-1} [g + \delta_x \cos(\eta_i) + \delta_y \sin(\eta_i)]^{3/2} \cos(\eta_i) \quad (16)$$

By assuming the elastic force in direction of δ_y to be zero, the first order approximation for δ_y is acquired. Taking partial derivate of the force with respect to the displacement in direction of δ_x , the stiffness of the bearing can be written as (Ragulskis et al. 1979 p. 48 – 49.)

$$k_{xx} = K \sum_{i=0}^{Z-1} \left[g + \delta_x \cos(\eta_i) - \frac{A}{cn} \sin(\eta_i) \right]^{1/2} \dots \\ \cdot \left\{ \cos(\eta_i) - \frac{ECn - AG(n-1)}{(cn)^2} \sin(\eta_i) \right\} \cdot \cos(\eta_i) \quad (17)$$

Where,

$$n = 3/2$$

$$A = \sum_{i=0}^{Z-1} [g + \delta_x \cos(\eta_i)]^{3/2} \sin(\eta_i)$$

$$C = \sum_{i=0}^{Z-1} [g + \delta_x \cos(\eta_i)]^{1/2} \sin^2(\eta_i)$$

$$E = \sum_{i=0}^{Z-1} [g + \delta_x \cos(\eta_i)]^{1/2} \sin(\eta_i) \cos(\eta_i)$$

$$G = \sum_{i=0}^{Z-1} [g + \delta_x \cos(\eta_i)]^{-1/2} \sin^2(\eta_i) \cos(\eta_i)$$

Expressing bearing stiffness not only in radial or axial directions, Lim & Chen (1990) proposed 6x6 stiffness matrix for rolling-element bearings to express non-in-plane motions of flexible casing plates. Diagonal component, radial stiffness, was verified to Gargiulo's (1980) analytical method and Kraus's (1987) experimental method. Proposed method had good agreement with both of the previously mentioned results by resulting into less than 2 % error when compared to Gargiulo's method. (Lim & Sheng 1990 p. 189.)

Numerical methods to calculate the bearing stiffness are based on linearization of bearing forces at given load. Rotor-Bearing Dynamics (RoBeDyn) toolbox for MATLAB, developed in LUT-university calculates the bearing stiffness matrix from the ball bearing forces and relative displacements between the inner and outer race by utilizing the Newton-Raphson iteration procedure. Figure 10 presents the relative displacements e_x , e_y and e_z in cross-sectional views of a ball bearing.

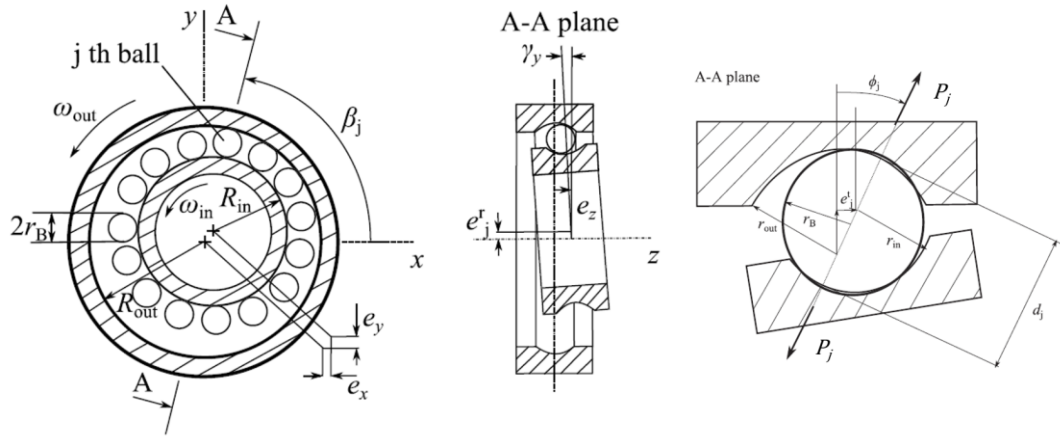


Figure 10. Cross-sectional view of ball bearing (Mod. Kurvinen et al. 2015, p. 245 – 246).

In RoBeDyn, the contact force of a single ball and races is described by Equation (1). Bearing forces and moments along x -, y -, and z -axis are described by Equation (18) (Sopanen & Mikkola 2003, p. 12).

$$\begin{aligned}
 P_x &= -\sum_{j=1}^Z P_j \cos \phi_j \cos \beta_j \\
 P_y &= -\sum_{j=1}^Z P_j \cos \phi_j \sin \beta_j \\
 P_z &= -\sum_{j=1}^Z P_j \sin \phi_j \\
 T_x &= -\sum_{j=1}^Z P_j (R_{in} + r_b) \sin \phi_j \sin \beta_j \\
 T_y &= -\sum_{j=1}^Z P_j (R_{in} + r_b) \sin \phi_j (-\cos \beta_j)
 \end{aligned} \tag{18}$$

Where, ϕ_j is the contact angle of j th ball, β_j the azimuth angle of j th ball, R_{in} is the inner raceway radius and r_b the ball radius (Figure 10). Displacements caused by a given load in directions e_x , e_y and e_z are solved with the Newton-Raphson iteration procedure, Equation (19) (Sopanen et al. 2019, p. 23).

$$\mathbf{e}^{(n+1)} = \mathbf{e}^{(n)} - (\mathbf{K}_T^{(n)})^{-1} \mathbf{Q}^{(n)} \quad (19)$$

Where, n is the iteration step, $\mathbf{K}_T^{(n)}$ is the tangent stiffness matrix and \mathbf{Q}^n the vector of bearing forces and external forces. $\mathbf{Q}^{(n)}$ is expressed by Equation 20 (Sopanen et al. 2019, p. 23).

$$\mathbf{Q}^{(n)} = \mathbf{Q}_b^{(n)} - \mathbf{Q}_{\text{ext}}^{(n)} \quad (20)$$

Where, $\mathbf{Q}_b^{(n)}$ is the vector of bearing forces and $\mathbf{Q}_{\text{ext}}^{(n)}$ is the vector of external forces. The tangent stiffness matrix is expressed by Equation (21). Based on the convergence criterion, Equation (22), the bearing stiffness matrix is the same as the tangent stiffness matrix at the last iteration step. (Sopanen et al. 2019, p. 24.)

$$\mathbf{K}_T^{(n)} = \frac{\partial \mathbf{Q}^{(n)}}{\partial \mathbf{e}^{(n)}} \quad (21)$$

$$|\mathbf{Q}| < 0,001 \cdot |\mathbf{Q}_{\text{ext}}| \quad (22)$$

Sheng et al. (2014) addressed the problem with numerical sensitivities in Jones-Harris ball bearing model when bearing dynamics are taken into account. To overcome this issue, Sheng et al. (2014) proposed an analytical method based on implicit differentiation and validated the method by comparing it to numerically calculated stiffnesses and to experimental measurements and models by other authors, such as Gargiulo's (1980) formula. When rotation speed was taken into account it resulted into lower stiffnesses with higher operation speeds, in which Gargiulo's (1980) method's resulted into higher stiffness values. (Sheng et al. 2014, p. 166 – 180.)

Guo & Parker (2012) presented a method to form stiffness matrix for rolling-element bearing by finite differences with the relative deflections and forces acquired from combined surface integral and finite element-model (FE). Presented method was used to determine bearing stiffness for multiple different rolling-element bearings and those results were compared to experimental measurements by other authors, computational programs and theoretical models. When compared to experimental measurements, proposed method had good agreement with acquired stiffnesses from previous studies. Guo & Parker (2012) noted that

the slight deviation between the results is due to boundary conditions that in the bearing model the outer surface of the outer race was modelled as a ground. (Guo & Parker 2012, p. 32 – 45.)

2.3.2 Experimental methods

Kraus et al. (1987) designed a test rig to study the stiffness of DGBBs by modal analysis. Test rig consisted of a rotor supported by two bearings in both ends, rotor was driven by a DC-motor connected via flexible coupling and the test rig was mounted to the base with flexible mountings. Excitation was given to the system by an excitation hammer and the displacement of the shaft was measured with a capacitive sensor. Kraus et al. (1987) studied the effect of axial preload, rotor speed and fit between the bearing and the housing to the equivalent stiffness of the bearings. Kraus et al. (1987) stated that greater bearing preload will decrease nonlinearities and will lead to better repeatability of the experiment. (Kraus et al. 1987, p. 235 – 240.)

Test rigs based on modal analysis have been then constructed with additional parameters to vary to study their effect to the bearing stiffness. Ali & García (2010) constructed a test rig with ACBBs with the possibility to study the effect of axial and radial bearing preload, oil viscosity and different fits between the outer race of the bearing and bearing housing, which in this study were transition and clearance fits. Figure 11 presents the experimental setup in their studies. (Ali & García 2010, p. 659 – 666.) In 2014 Jacobs et al. presented test rig that can apply static and dynamic load cases in axial and radial direction of the test bearing by six different actuators (Jacobs et al. 2014, p. 103 – 113).

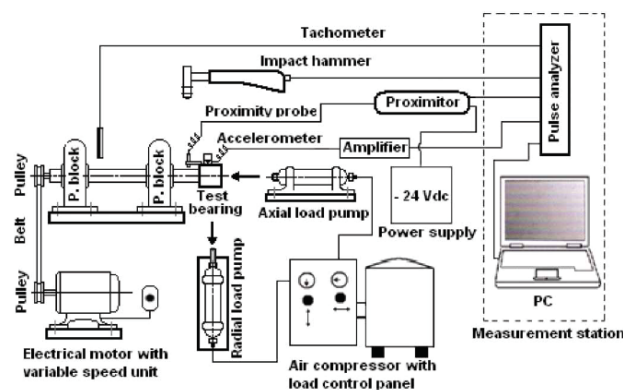


Figure 11. Experimental setup in modal analysis based stiffness estimation (Ali & García 2010, pp. 660).

Previously described methods based on modal analysis can only be used to acquire radial or axial stiffness. Experimental methods to acquire full 6x6 stiffness matrix has been studied by Knaapen (1997) to overcome the issues in previous attempts to form the full stiffness matrix experimentally, based on efforts by previously mentioned Lim & Chen (1990). However, in the study cross-coupled stiffness terms were not possible to be determined. (Knaapen 1997, p. 9 & 37.) Test rig setup by Knaapen (1997) is presented in Figure 12.

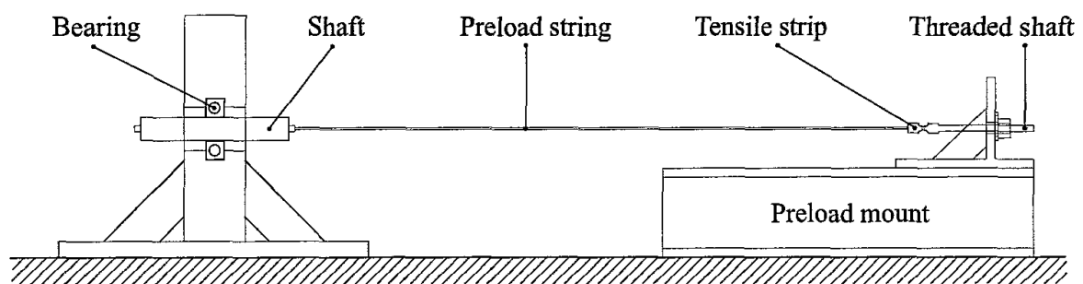


Figure 12. Experimental setup for full 6x6 stiffness matrix estimation (Knaapen 1997, p. 19).

Tiwari, R & Vyas (1995) presented a method to estimate the non-linear bearing stiffness without the need to know the excitation forces. A test rig used in the study, consisted of a shaft with a disk in the middle and was supported by two ball bearings in each end which were mounted on two bearing housing blocks. Vibrations were measured in vertical and horizontal directions with two accelerometers from one of the bearing housing. Displacement data was then used to calculate the linear natural frequency and non-linear stiffness parameters (Tiwari, R. & Vyas 1995, p. 229 – 239).

Tiwari, M. et al. (2002) studied the stiffness of SKF 6002 DGBBs supporting a rigid Jeffcott-rotor. Stiffness estimation in horizontal and vertical directions were acquired by analyzing the frequency spectra of displacement of the rotor. Two natural frequencies with 2X or higher harmonic were estimated to acquire the corresponding horizontal and vertical stiffness. (Tiwari, M. et al. 2002, p. 247.)

Previously mentioned study by Bauer & Werner (2016) can also be included in the experimental methods. In the study, the vibration data in vertical and horizontal directions

of a 650 kW induction motor during 0 – 1800 RPM (revolutions per minute) run-up measurement were gathered. By waterfall plot-analysis the natural frequency of the first bending mode of the rotor was acquired and the stiffnesses in vertical and horizontal directions in the computer model of the rotor were altered to get the similar result for the natural frequency of the first bending mode. (Bauer & Werner 2016, p. 1 – 9.)

2.3.3 Main findings from the literature review

Main findings from the literature review indicate that bearing stiffness estimation is nowadays focused on numerical methods. Numerical methods require number of inputs and computational power, but the results are better compared to analytical methods that are easy to use but can only be used for a rough estimate. Main advantages in experimental methods are that the stiffness is measured from an actual system with accurate description, for example of the dynamic behavior of the rotor, fit between the bearing and the housing and the bearing temperature. Disadvantages of experimental methods can be the cost of the instruments to acquire the required data and the installation time, given that the system is not equipped with the required instruments already.

3 METHODS USED FOR BALL BEARING STIFFNESS EVALUATION

This chapter presents the methods used in the experimental part to estimate the bearing stiffness. The chapter presents the used software, description of the test rig setup and measurements of different components of the test rig. Lastly, a measurement procedure to estimate the bearing stiffnesses is presented.

3.1 Software

The accuracy of the bearing stiffness estimation from experimental approach is verified by stiffness values acquired computationally by using BearinX Online Shaft Calculation (ver. 8.0.5071) and MATLAB (2018b) with Rotor-Bearing Dynamics (RoBeDyn) toolbox (ver. 2.2) developed in LUT-university.

BearinX is a product by Schaeffler Group, manufacturer of FAG-bearings. BearinX can be used with bearings by FAG and it is possible to calculate the 5x5 stiffness matrix for each bearing in the system. RoBeDyn-toolbox bases the calculation of the stiffness matrix from force components calculated from the relative displacements between the inner and outer races in three translational directions. Toolbox describes the contact stiffness based on the Hertzian contact theory. Input parameters in the toolbox are the bearing dimensions, material properties and clearances. The calculation procedure is based on Newton-Raphson iteration and outputs the tangent stiffness matrix.

3.2 Deep-groove ball bearing geometry measurements

Manufacturer provides dimensions for the assembled bearing and accurate information of internal geometries such as ball diameter or inner and outer groove radii are challenging to find or not provided by manufacturer. The DGBBs 6309-2Z and 6209-C-2HRS by FAG that are used in the test rig had no available information of the internal geometries that are required for RoBeDyn-model, thus bearing dimensions are measured. All geometrical measurements of DGBBs are conducted by VTT Technical Research Centre of Finland Ltd., in Espoo.

Clearance of the bearing is measured with Tesa Modul measurement device with an inductive sensor and ball diameter is measured with Mahr Precimar PLM 600-E measurement device. Ball diameters are measured from half of the balls in the bearing. Outer and inner geometries of the bearing are measured with Mitutoyo Legex 9106 coordinate measurement machine (CMM).

The measurements are done for new bearings to avoid inaccuracies in results if the bearing would have been damaged during the de-assembly of the motor. De-assembly of the bearings is done by removing the bearing shield and the cage to push the balls out from the grooves. Conformity ratio of inner and outer race is the ratio of groove radius to ball diameter. Typical value for conformity ratio is 0,52 yet it can be between 0,52 and 0,54 (Hamrock & Anderson 1983, p. 8). Figure 13 presents the de-assembled bearings, Figure 14 presents the measurement of the ball diameter and Figure 15 presents the measurement of outer groove radius.



Figure 13. De-assembled bearings, 6209-C-2HRS on the left and 6309-2Z on the right.

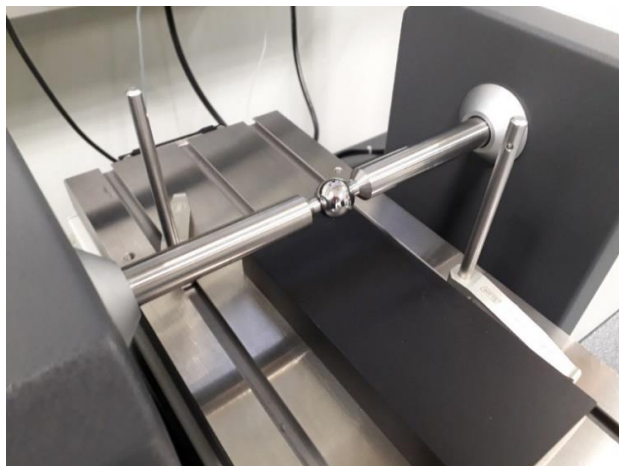


Figure 14. Ball diameter measurement.

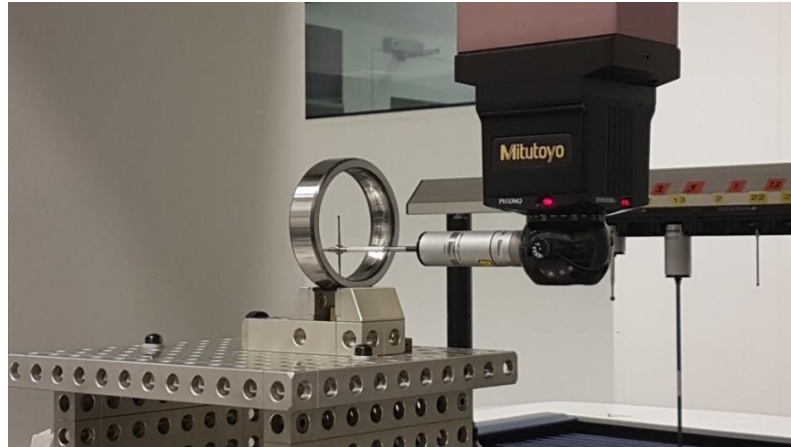


Figure 15. Measurement of outer groove radius.

DGBB parameters used in RoBeDyn-model are presented in Table 1. For comparison, DGBB dimensions provided by the manufacturer are included in parenthesis. Material properties of the bearing were not measured, thus values used in the model are approximations. Material used by FAG in rolling-element bearings is normally 100Cr6 (Schaeffler 2015) which has modulus of elasticity of 210000 MPa and Poisson's ratio of 0,3 (OVAKO 2019). Diameter of the ball is an average value of ball diameter measurements. All geometrical measurements of DGBBs are presented in Appendix I. Bearings are attached to the ground in RoBeDyn- and BearinX-models, i.e. outer race is fixed.

Table 1. Parameters used in RoBeDyn-model, values given by manufacturer in parenthesis for comparison (Schaeffler 2019d; Schaeffler 2019a).

Parameters	FAG 6309-2Z	FAG 6209-C-2HRS
Inner diameter of inner race, d [mm]	44,9917 (45)	44,99969 (45)
Outer diameter of outer race, D [mm]	99,9933 (100)	84,9981 (85)
Radial clearance, c_{dy} [mm]	0,030	0,028
Ball diameter, D_b [mm]	17,4582	11,9033
Number of balls, Z	8	10
Race conformity ratio of inner race, r_{in}/D_b	0,51	0,52
Race conformity ratio of outer race, r_{out}/D_b	0,54	0,55
Modulus of elasticity, E_a and E_b [MPa]	210000	210000
Poisson's ratio, ν_a and ν_b	0,3	0,3

3.3 Test rig and measurement setups

The motor used in measurements is ABB M3BP 160MLA 4 IMB3/IM1001 3-phase 11 kW induction motor. The rotor is supported from the DE by FAG 6309-2Z DGBB and from the NDE by FAG 6209-C-2HRS DGBB. Internal clearance of both of the bearings is C3 and NDE bearing is axially free while DE bearing is fixed. Relative displacements of the rotor with respect to the bearing shields are measured in x - and y -directions by two capacitive displacement sensors developed in LUT-university, one mounted to the DE and other to the NDE. Resolution of the capacitive sensor is $0,16 \mu\text{m}$. The use of the capacitive sensor, which was originally designed for active magnetic bearing applications, in electrical machines with DGBBs was studied by Pelli (2018) (Pelli 2018, p. 1 – 73). Test rig and x - and y -directions from DE are presented in Figure 16.

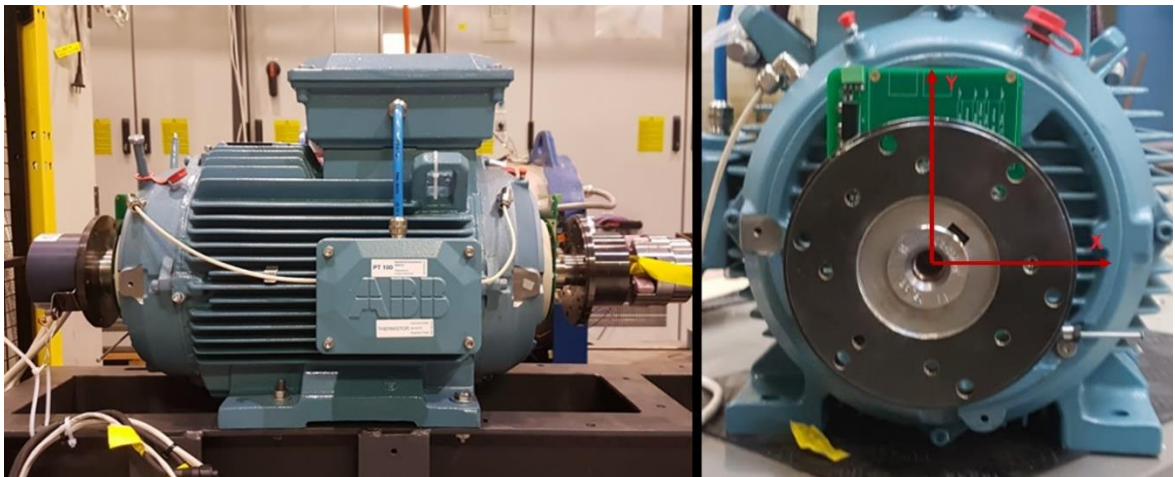


Figure 16. Test rig and the x - and y -directions from DE.

Rotation speed of the motor is controlled with ABB ACS800 variable frequency converter (VFC). Acceleration is measured in x -direction from DE bearing housing by IMI 622B01 accelerometer. Specifications of the accelerometer are presented in Table 2. Incremental encoder (serial number: 38280059) by Leine & Linde is used to measure the angle of the shaft and is mounted at the NDE of the motor, resolution of the encoder is $0,352$ degrees. Temperatures of the bearings are monitored with PT100 resistance thermometers mounted inside the bearing shields. Total of 19 temperature samples are taken during one measurement cycle. Length of one measurement cycle is between 13 s and 26 s. The sensors are connected to ABB AC500-CMS programmable logic controller (PLC) via EtherCAT connection.

Table 2. 622B01 accelerometer data (PCB Piezotronics 2019).

Performance	Value
Sensitivity [mV/(m/s ²)]	10,2
Measurement range [m/s ²]	± 490
Non-linearity [%]	± 1
Frequency range [Hz]	0,58 – 6000 (± 5 %) 0,42 – 10000 (±10 %) 0,2 – 15000 (± 3 dB)
Broadband resolution [µm/s ²]	490 (from 1 to 10000 Hz)

Sampling rate of the capacitive displacement sensors is 20 kHz and 50 kHz for accelerometer and rotary encoder. The test motor was disassembled for the measurements in the facilities of LUT. Measurements included the measurement of the bore diameter and surface roughness of the bearing shields and modal analysis of the rotor.

3.3.1 Geometrical measurements

Bore diameters of DE-, NDE-shields and rotor diameter from bearing surface were measured with a Bowers EG5 micrometer. The accuracy of the micrometer before the measurements was verified by using a calibration block. Surface roughness of the bore was measured with Mitutoyo Surftest 201 from a single point and was calibrated beforehand. Figure 17 presents the measurement setup. Geometrical measurements are presented in Table 3 which includes the measured diameters of the outer races of the bearings in parenthesis and the calculated clearances between the bearing housing and the bearing outer race. Surface roughnesses are presented in Appendix I.

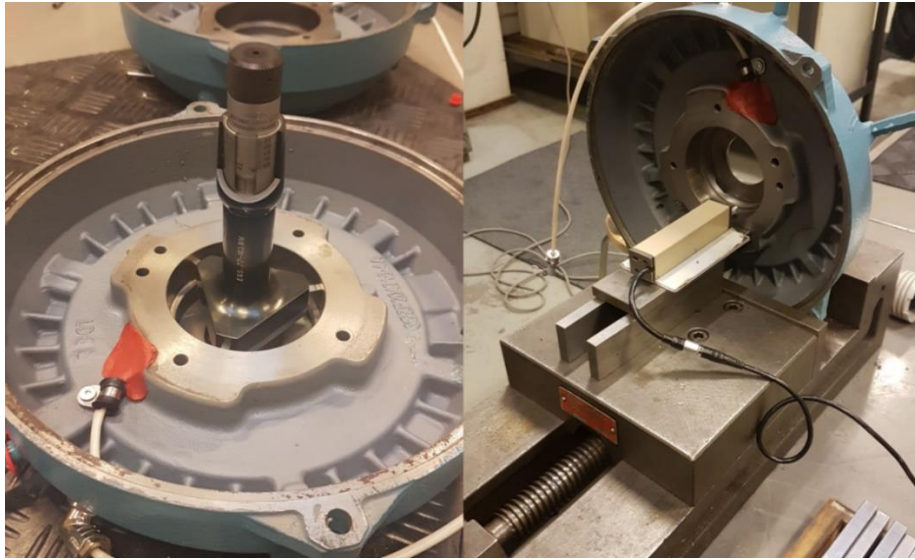


Figure 17. Bore diameter measurement (left) and surface roughness measurement (right) for NDE-shield.

Table 3. Bore and rotor diameters.

Part	Diameter [mm]	Clearance [mm]
DE-shield	100,0 (99,9933)	0,0067
NDE-shield	85,0115 (84,9981)	0,0134
Rotor	45,0014	–

3.3.2 Modal analysis of the rotor

Free-free modes of the rotor were determined with modal analysis. Modal analysis was done with a scanning vibrometer by Polytec, including a PSV-500 scanning head and OFV-505 reference laser. Excitation to the rotor was given with an AS-1220 excitation hammer by Alpha Solutions. Rotor was supported with ropes that were located at the bearing locations. Measurements were done in two different planes to inspect the influence of geometrical asymmetry due to e.g. keyholes in the shaft. After measurements in one plane, x -plane, the rotor was rotated 90 degrees to measure the y -plane. Measurement setup is presented in Figure 18 and directions of x - and y -axis are presented in Figure 19.



Figure 18. Modal analysis set up.



Figure 19. x - and y -axis orientation from NDE of the rotor.

Measurement settings were defined in PSV 9.2 Acquisition-software. FFT-measurement (Fast Fourier Transform) mode was used with three repeated measurement of each defined points. Modal analysis was carried out in frequency range of 0 Hz to 2500 Hz. Frequency that the hammer used for excitation was 0,2 Hz as a square wave input with 4,8 V amplitude. The sensitivity of reference laser and scanning laser were adjusted during initial measurement setup to avoid overshoots. For the scanning and reference laser velocity of 50 mm/s was used.

Measurement points were marked with a reflection point to avoid scattering of the laser light, total of 12 measurement points were used. After marking the points, 2D- and 3D-alignment was done in the program. Due to defined settings, the hammer excited the rotor every five seconds and every point was measured three times. Figure 20 presents the view of the program. Operational Deflection Shapes (ODS) analysis was also conducted for the motor at 1500 RPM. Results for modal analysis are presented in Appendix II.

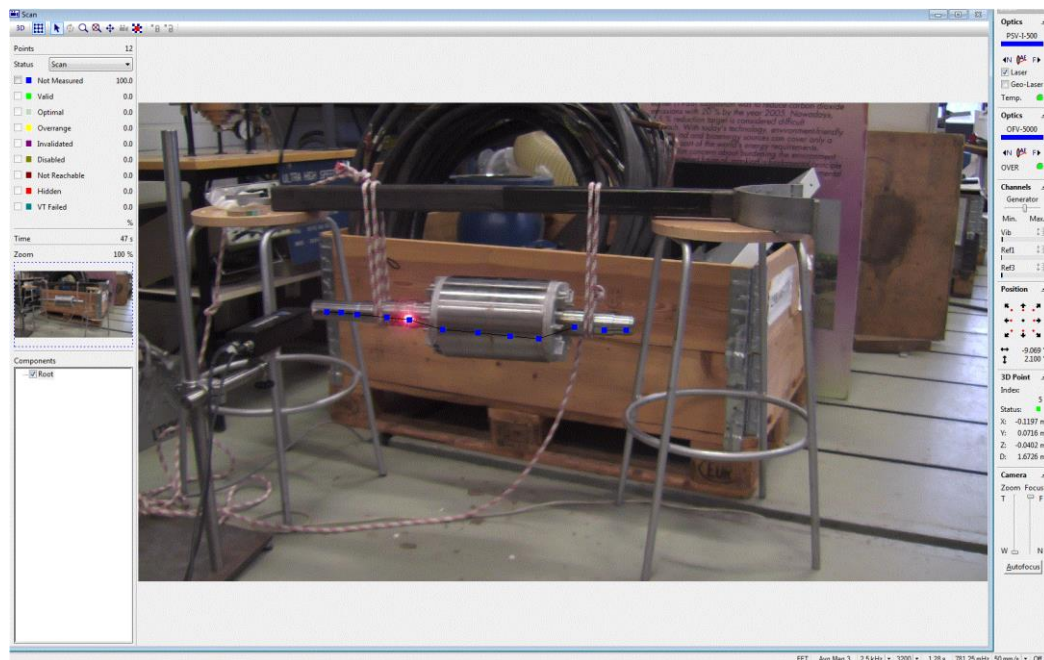


Figure 20. Screenshot from PSV 9.2 Acquisition –software.

3.3.3 Measurement procedure of shaft displacement measurements

Shaft displacement is measured with different static unbalance conditions. A force caused by a rotating unbalance is defined by Equation (23).

$$F_{unbalance} = me\omega^2 \quad (23)$$

Where m is mass of the unbalance mass (kg), e is the distance of the unbalance mass from axis of rotation (m) and ω is the rotation speed (rad/s). By determination of the displacement and phase caused by the rotating unbalance (1X-vibration) of two different unbalance cases from the capacitive sensor and tachometer data, displacement vectors \mathbf{q}_1 and \mathbf{q}_2 (Figure 21) can be drawn. Difference vector \mathbf{dq} represents the displacement caused by the change in force and thus stiffness can be calculated by using Equation (5).

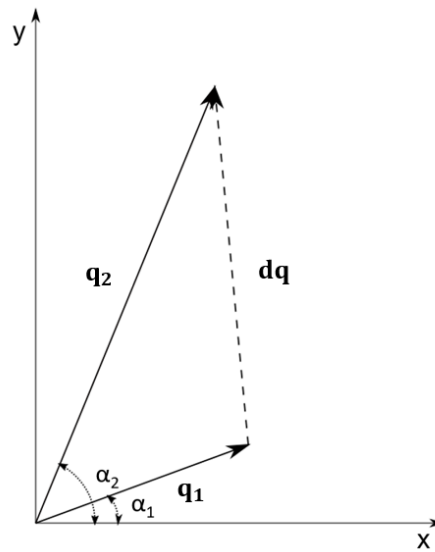


Figure 21. Vector drawing.

Three parameters to vary in the study were defined to be the rotation speed of the rotor, axial preload of the NDE-bearing and the magnitude of centrifugal force which was adjusted by mass unbalance. Rotation speed of the rotor is varied from 500 RPM to 4500 RPM. Axial preload of the NDE bearing is initially 445 N which is applied by a wave spring with 229 N/mm spring constant. Axial preload in the measurements is varied by placing sheet metal shims with 0,1 mm and 0,3 mm thicknesses between the NDE bearing shield and the wave spring. Figure 22 presents the adjustment of preload.

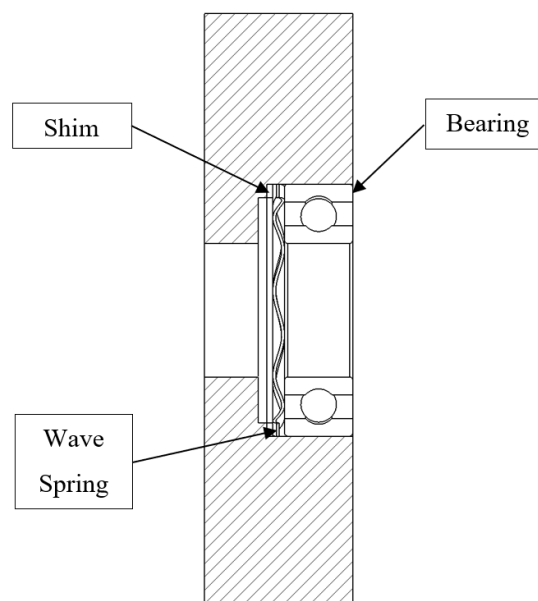


Figure 22. Illustration of the adjustment of preload.

Mass unbalance is adjusted by nuts and bolts which are mounted to coupling hubs at DE and NDE. Mass of the DE coupling hub is 3,5 kg and 1,8 kg for the NDE coupling hub, 8 mm diameter holes are machined on both of the hubs that are located 65 mm from the center of the hub. Weight of the unbalance masses and hubs are measured with EK-12KA scale by A&D Company. DE hub is mounted backwards on the shaft to move the location of unbalance mass closer to the DE-bearing. At DE the location of mass unbalance is approximately 96,05 mm from the DE-bearing centerline and at NDE the location of the mass unbalance is approximately 92,50 mm from the NDE-bearing centerline. Drawing of the setup is presented in Appendix III. Unbalance masses are mounted 180 degree from the location of the keyway. Phase between the DE and NDE masses is approximately zero. Figure 23 presents the mounted coupling hubs on the shaft.

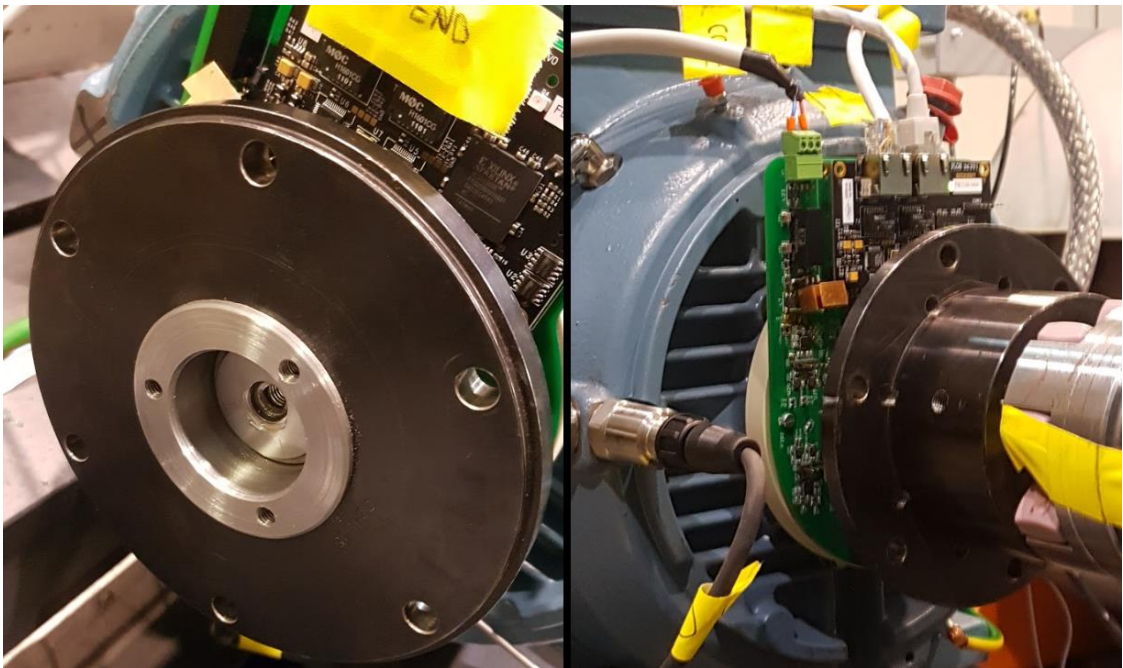


Figure 23. Coupling hubs to adjust the unbalance at NDE (left) and DE (right).

Measurements are done in speed range of 500 RPM to 4500 RPM with 1000 RPM steps. Tested unbalance masses are 14, 22, 30 and 37 grams, measurements with zero added unbalance is also measured. Used NDE preloads include 445 N, 673 N and 788 N preloads, 445 N is the initial preload of the bearing while 673 N and 788 N are acquired with shims with total thickness of 1 mm and 1,5 mm, respectively. In the current setup capacitive sensors were not able to measure both DE and NDE simultaneously, thus the total number of measurement points is 150. Measurements are done by first accelerating the rotor to 4500

RPM and then decelerating the rotor in 1000 RPM steps, last measurement being the 500 RPM measurement. Temperatures are recorded from each measurement points, thus bearings are not allowed to cool down between the measurements except when the preload is adjusted. No additional lubrication is added to the bearings during the preload adjustment.

Due to the incremental sensor the keyway of the shaft is aligned with a reference point located at the top of the motor frame prior to the measurements. After measurements for 445 N and 673 N preloads the frame in which the motor was mounted, was mounted to the steel bed from three points to limit the frame movement during measurements. Measurements with 788 N preload were thus measured with mounted frame. Location of mounting points are presented in figure 24.

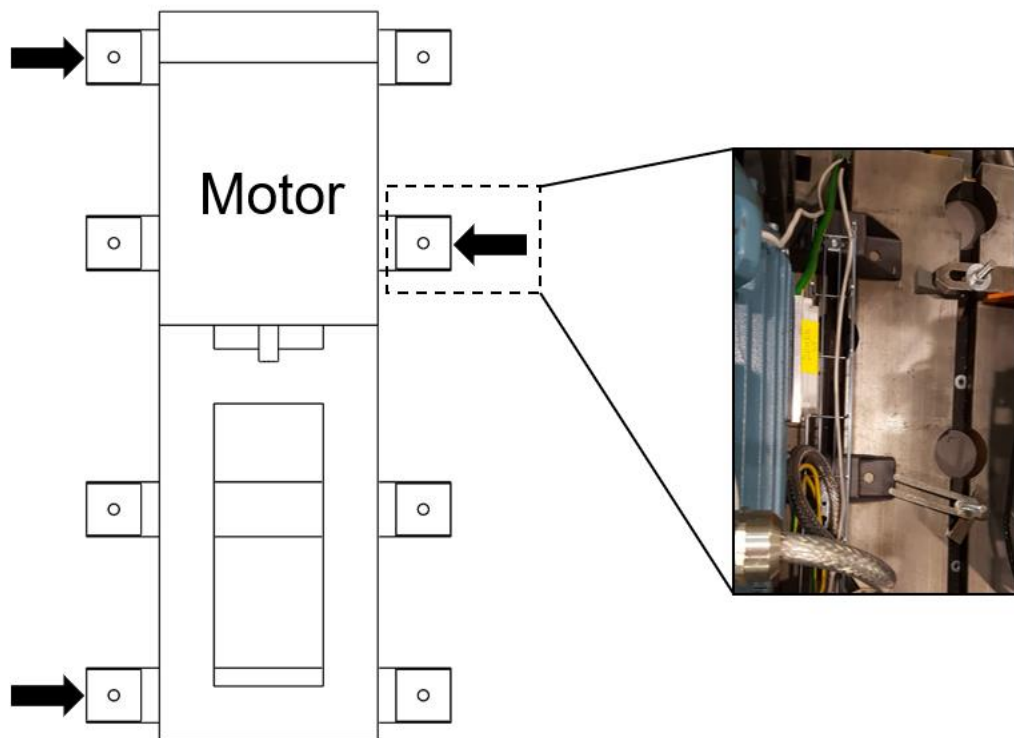


Figure 24. Frame mounting for 788 N preload measurements.

3.3.4 Post-processing

For data post-processing MATLAB (2018b) is used. Acquired raw displacement data is filtered by using bandpass-filter to acquire displacement caused by unbalance. Bandpass cut-on and cut-off frequencies are calculated from rotation speed data of tachometer with $\pm 0,5$ Hz tolerance. Mechanical run-out (MRO), which is due to un-concentricity of the

measurement surface, is compensated from the measurements by using 500 RPM measurements with no added unbalance.

In MRO compensation the 1X-vector of slow roll data, which in this case is the previously mentioned 500 RPM data, is subtracted from other measurement's 1X-vector. Run out compensation is presented in Figure 25, in which the solid purple line presents slow roll measurement and red solid line presents un-compensated measurement. Vector subtraction yields a new vector, solid blue line, which is the run-out compensated measurement.

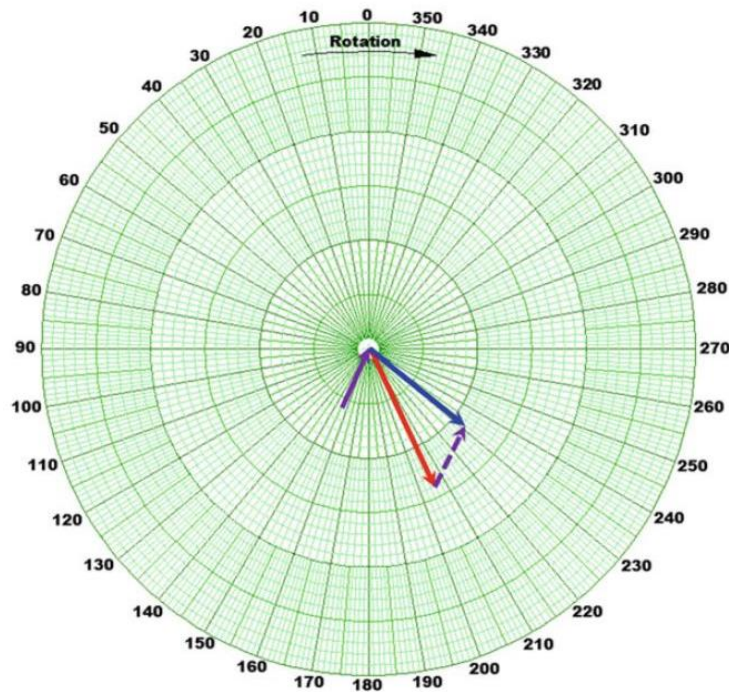


Figure 25. Run-out compensation (Subbiah & Littleton 2018, p. 162).

In the post-processing the tachometer data is downsampled to 10 kHz and then upsampled to 20 kHz. During initial measurements it was verified that there is no movement of the tachometer that would cause an error to the determination of the phase. Figure 26 presents displacements in x - and y -direction as a function of the rotor angle. Graph at top presents the raw data and bottom graph presents average displacement at certain rotor angle. It can be seen from the figure that the tachometer is mounted properly.

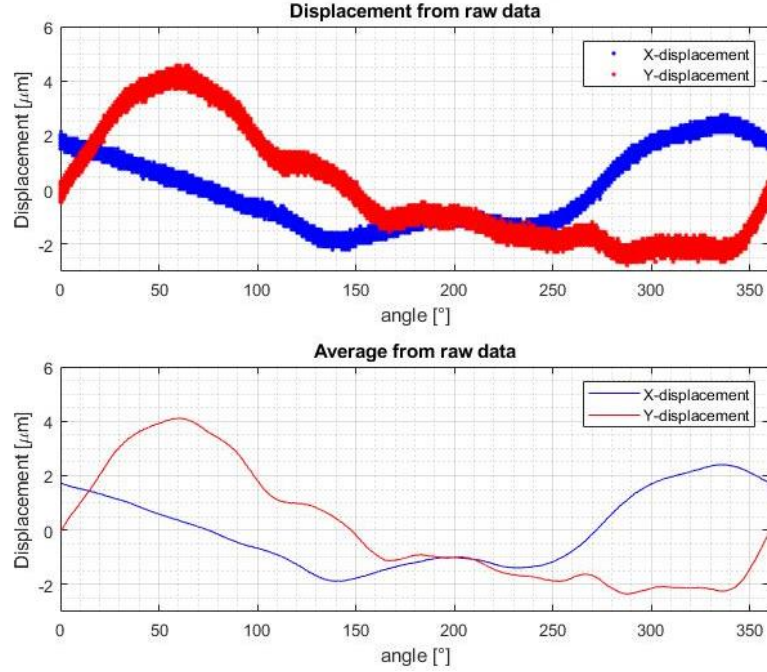


Figure 26. DE measurement with no added unbalance at 1500 RPM.

FFT is used to acquire amplitudes at 1X-frequency which are caused by the rotating unbalance. Frequency resolution in FFT is defined by Equation (24).

$$\Delta f = \frac{f_s}{N} \quad (24)$$

Where f_s is sampling rate [1/s] and N is the number of samples. According to the Equation (24) resolution increases with the increase of number samples when the sampling rate is constant. Increase in number of samples is achieved by increasing the length of the measurement. Length of the measurements is varied from 13 s to 26 s, which correspond to resolution from 0,0769 to 0,0385 with 20 kHz sampling rate.

Phase of the 1X-vector is determined from the angle of the rotor at which the maximum amplitude of displacement occurs. From the measured data maximum displacement at each revolution of the rotor is taken into account and from the acquired data set a median value is taken that is the phase. In Figure 27 is presented NDE measurement with 14 g unbalance at 1500 RPM. Left side in the figure present the phase determination of measurements in x -direction and on the right are phase determination in y -direction measurements. At the bottom of the figure are presented histograms of the results during the complete

measurement, from 0 s to 12,7502 s, and at the top are shown displacements as a function of time, from 2 s to 2,25 s. Tachometer data is presented with green line, tachometer data varies between 0 to 360 degrees and is scaled down in the figure to vary between 0 to 3,6 degree. Displacement and tachometer data graphs were used to validate the method to determine the phase.

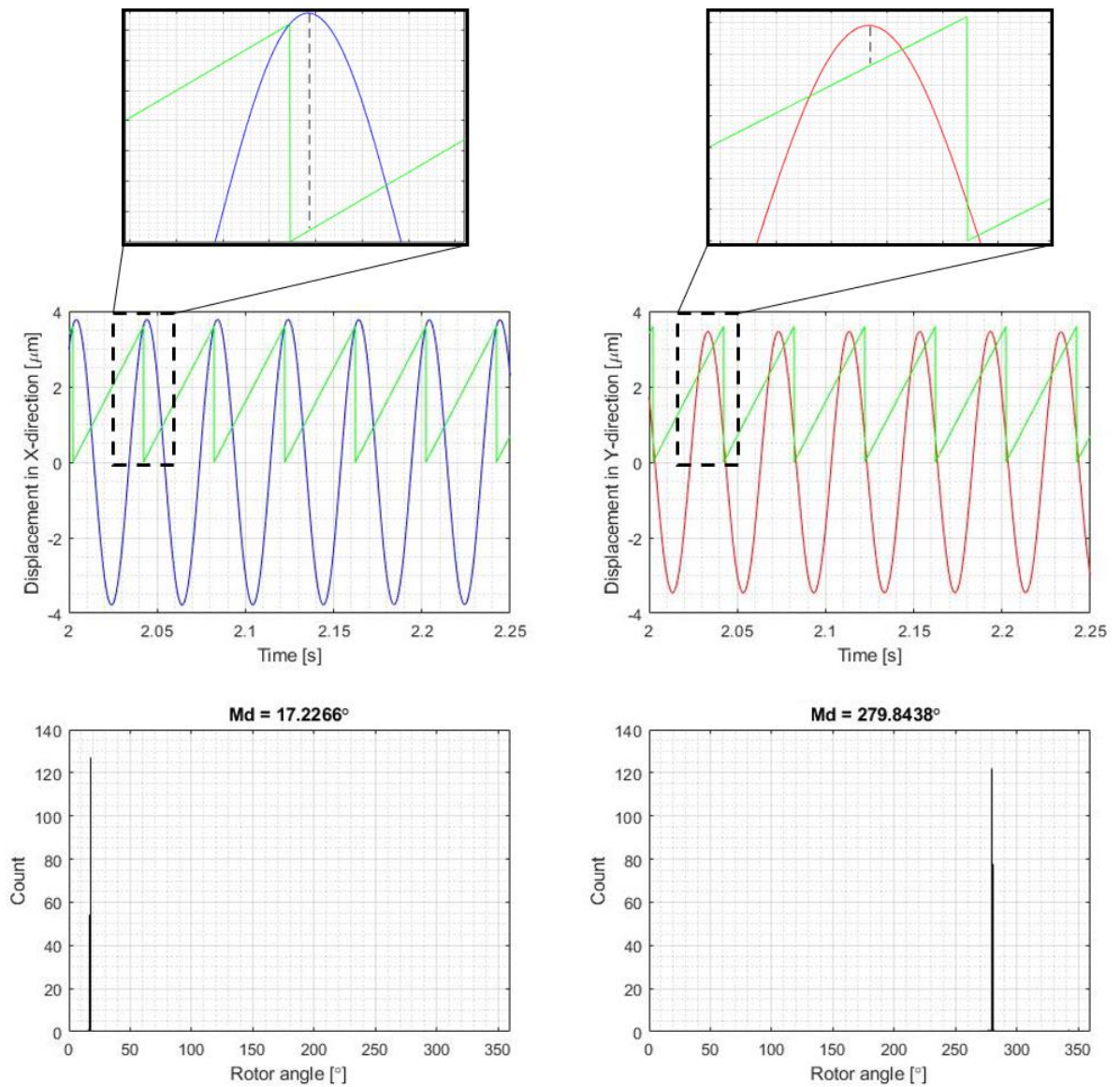


Figure 27. Phase determination of NDE-bearing with 14 g unbalance at 1500 RPM.

4 ANALYTICAL, NUMERICAL AND EXPERIMENTAL RESULTS OF DEEP-GROOVE BALL BEARING STIFFNESS ESTIMATION

This chapter presents firstly the analytical and numerical methods and then the experimental results for shaft displacement measurements and then stiffnesses acquired from those measurements. Lastly comparison between the results are presented.

4.1 Numerical and analytical results

Table 4 presents the stiffnesses of k_{yy} acquired numerically from RoBeDyn and BearinX. Stiffnesses are acquired from slope of a line of best fit of a load-displacement scatterplot. Stiffnesses of k_{xx} are the same as k_{yy} due to the boundary condition in the computational model (fixed outer race). Table 4 also includes results for stiffnesses by using Gargiulo's analytical method, Equation (6). In Gargiulo's equation same parameters are used as in RoBeDyn-model (Table 1), contact angle α is assumed to be zero rad.

Table 4. Numerical and analytical results for stiffnesses with different preloads.

Method	Preload [N]	NDE-bearing 6209-C-2HRS k_{yy} [N/mm]	DE-bearing 6309-2Z k_{yy} [N/mm]
RoBeDyn	445	189992	208133
	673	214982	235889
	788	224971	247011
BearinX	445	165134	164613
	673	183537	180350
	788	188996	186534
Gargiulo	-	61764	60475

With RoBeDyn- and BearinX-models the stiffness can be seen to increase as the preload increases. With the RoBeDyn-model stiffnesses are greater when compared to BearinX-results, difference between the two methods increases as the increase of preload. With the BearinX-model there can be seen that the NDE-bearing has greater stiffness than the DE-

bearing. By comparing the numerically acquired results with 455 N preload case to Gargiulo's analytical method, which does not take into account the preload and assumes zero radial clearance, results are 67 % – 71 % lower than with RoBeDyn and 63 % lower than with BearinX-software.

4.2 Shaft displacement measurements

This chapter is divided into two subchapters presenting the load-displacement curves of NDE- and DE-measurements, respectively. Temperatures of the bearings during measurements for NDE-bearing are presented in Table 5 and for DE-bearing in Table 6. Shaft-displacement measurements without run-out compensation are presented in Appendix IV. Appendix IV includes the amplitude of 1X-vector in μm and the phase in degrees.

Table 5. Temperatures of NDE-bearing in Celsius (C°).

Preload [N]	Unbalance Mass [g]	Rotation Speed [RPM]				
		500	1500	2500	3500	4500
445	0	35,2	-	33,5	33,4	33,0
673	0	30,0	29,5	28,9	28,1	27,0
	14	30,9	30,8	30,8	30,8	30,1
	22	33,8	33,9	34,1	34,3	33,4
	30	27,0	26,9	26,5	25,9	24,5
	37	31,9	32,0	32,0	32,0	30,9
788	0	25,0	24,6	24,2	23,4	22,0
	14	34,4	34,6	34,7	34,8	33,7
	22	31,1	31,2	31,3	31,4	30,5
	30	31,6	31,7	31,8	31,8	30,4
	37	27,2	27,1	27,1	26,8	25,4

Table 6. Temperatures of DE-bearing in Celsius (C°).

Preload [N]	Unbalance Mass [g]	Rotation Speed [RPM]				
		500	1500	2500	3500	4500
445	0	-	31,1	31,4	-	30,0
673	0	-	24,0	24,4	24,8	24,9

Table 6 continues. Temperatures of DE-bearing in Celsius (C°).

673	14	31,5	31,8	32,2	31,8	31,3
	22	32,4	32,6	32,7	32,8	32,3
	30	28,8	29,0	28,8	28,3	27,1
	37	32,3	32,6	32,6	32,5	31,6
788	0	28,5	28,7	28,8	28,5	27,1
	14	32,2	32,5	32,7	32,7	31,5
	22	31,4	31,7	31,9	32,0	30,8
	30	28,7	28,8	29,1	28,8	27,2
	37	29,1	29,5	29,9	30,1	28,3

4.2.1 Non-Drive End

Figures 28 and 29 present the displacement of the shaft in NDE with 445 N preload in x - and y -direction, respectively. Figures include the stiffnesses k_{xx} and k_{yy} acquired from the slope of the line of best fit and the correlation coefficient r_c .

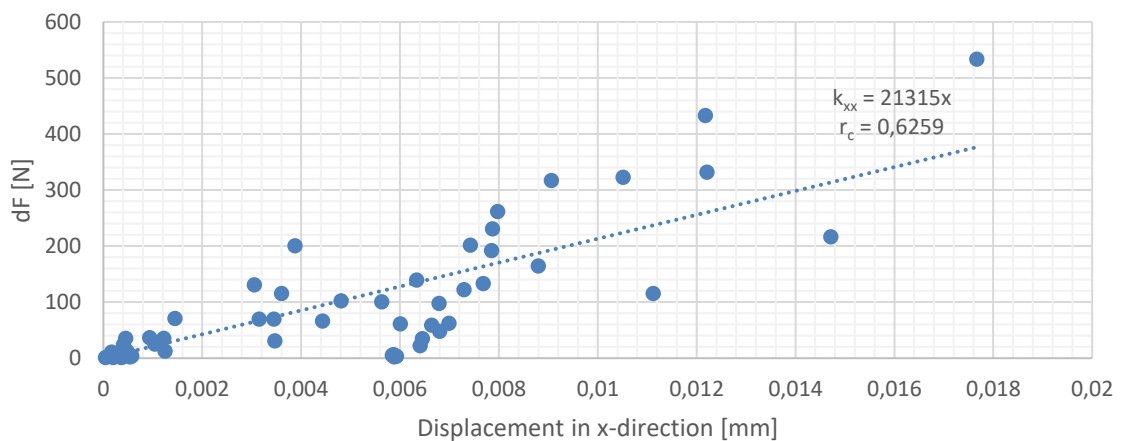


Figure 28. Load-displacement curve of NDE in x -direction with 445 N preload.

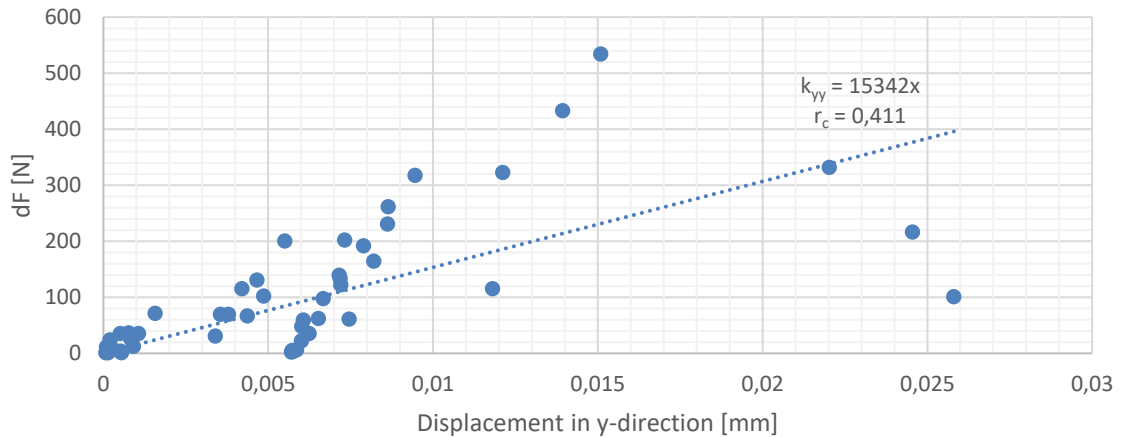


Figure 29. Load-displacement curve of NDE in y -direction with 445 N preload.

Figure 30 presents the displacement of the shaft in NDE in x - and y -directions as a function of rotation speed with different preloads. With 445 N preload there can be seen approximately 6 μm displacement at 500 RPM in both x - and y -directions. This is due to the approximate 180 degree phase difference between the run-out measurement and measurements with added unbalance. Displacements in both directions increase as the rotation speed increases due to the force caused by the unbalance. However, with 14 g unbalance mass there can be seen that the displacement decreases at 3500 RPM in both directions.

With 673 N preload the displacements are closer to 0 μm at 500 RPM and increase with the increase of rotation speed and added unbalance. However, there can be seen that this is not the case with 37 g measurement where in x -direction the displacement is 4,2 μm and in y -direction 2,8 μm at 500 RPM. Additionally, the displacements in x -direction stay nearly constant till 3500 RPM where displacements decrease. Similar behavior can also be seen in y -direction where displacements stay constant till 2500 RPM. In Appendix IV there can also be seen that the amplitudes prior to the run-out compensation are smaller than with smaller unbalances and there is a great phase difference between 37 g measurements and run-out measurement. With 788 N preload the behavior of displacements in x - and y -directions are closer to what is expected.

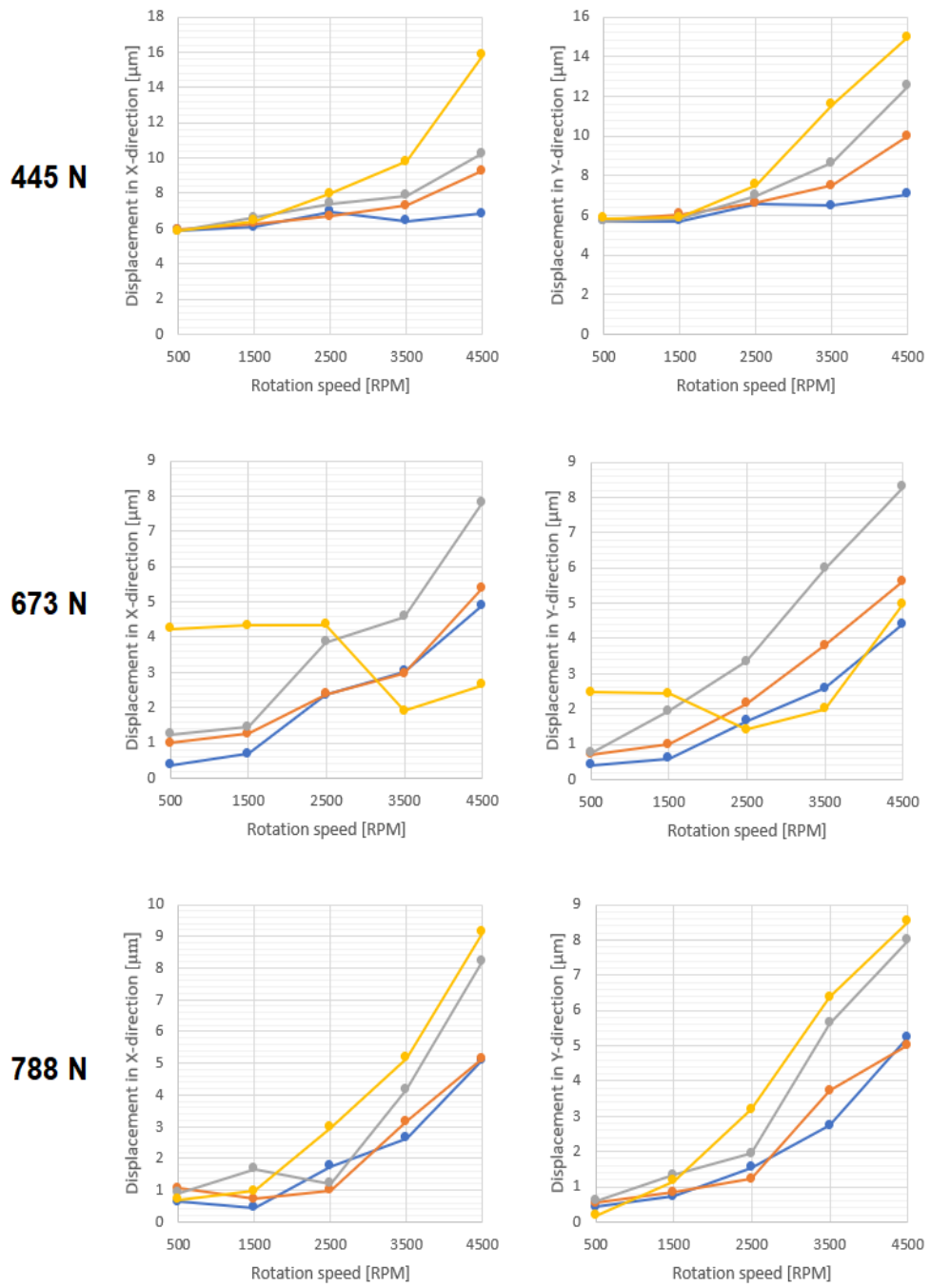


Figure 30. Displacements of NDE as a function of rotation speed (blue line represents 14 g unbalance, orange line 22 g unbalance, grey line 30 g unbalance and yellow line 37 g unbalance).

4.2.2 Drive-End

Figures 31 and 32 present the displacement of the shaft at DE with 445 N preload in x - and y -direction, respectively. Figures include the stiffnesses k_{xx} and k_{yy} , acquired from the slope of the line of best fit and the correlation coefficient r_c .

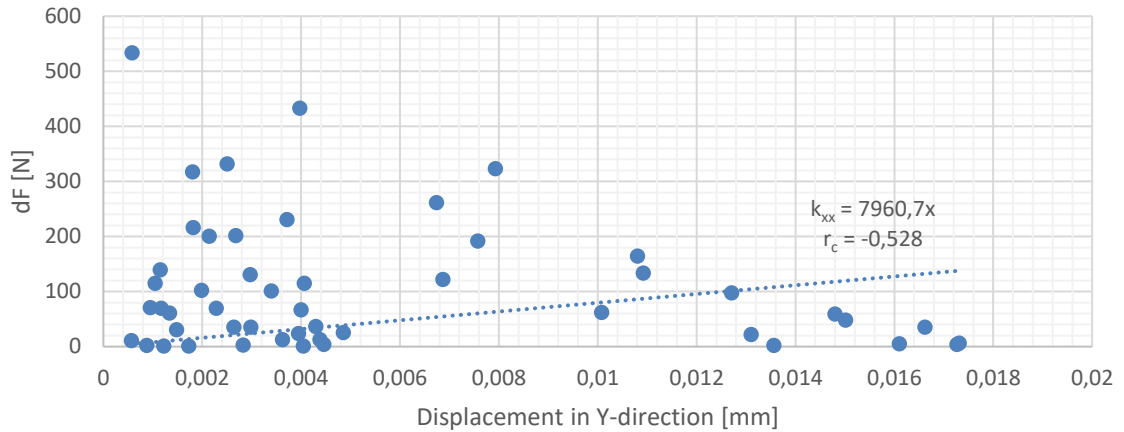


Figure 31. Load-displacement curve of DE in y -direction with 445 N preload.

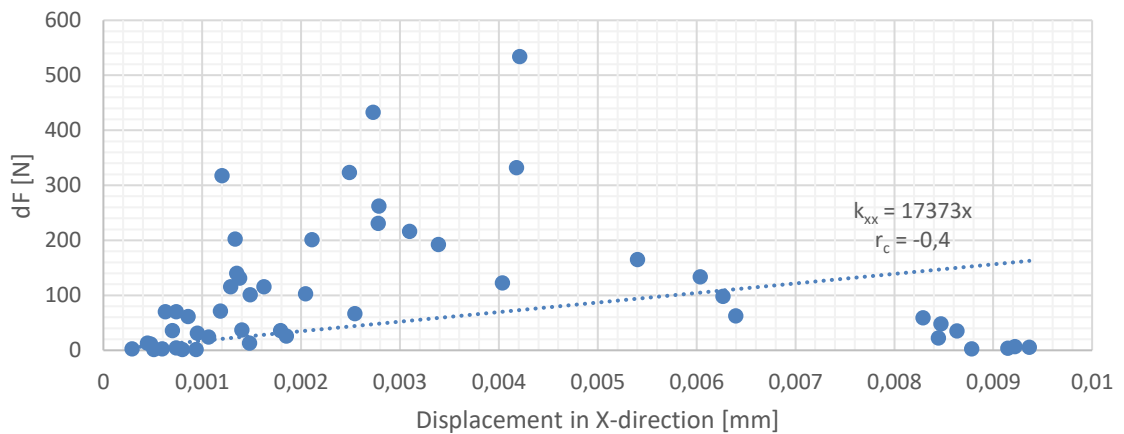


Figure 32. Load-displacement curve of DE in x -direction with 445 N preload.

Figure 33 presents the displacements of the shaft at DE in x - and y -directions as a function of rotation speed with different preloads. With 445 N preload the displacement seem to decrease as the increase of rotation speed also similarly with the NDE there is approximately 180 degree phase difference between the run-out measurement and measurements with added unbalance. With 673 N preload in x -direction the displacements seem to behave as expected, however with 37 g measurement the displacements are much greater compared to

others. From Appendix IV there can also be seen that there is a great difference between phases between the run-out measurement and 37 g measurements. In y -direction there can be seen that the displacements do not follow a similar trend as in x -direction. With 788 N preload the displacements in x -direction behave more like to expect, however with 14 g unbalance there can be seen a decrease in displacement amplitude at 2500 RPM and with 22 g unbalance at 1500 RPM. In y -direction there can be seen drop in displacement amplitude at 2500 RPM with every unbalance, except with 37 g. With rotation speeds greater than 2500 RPM the displacements increase with every unbalance cases.

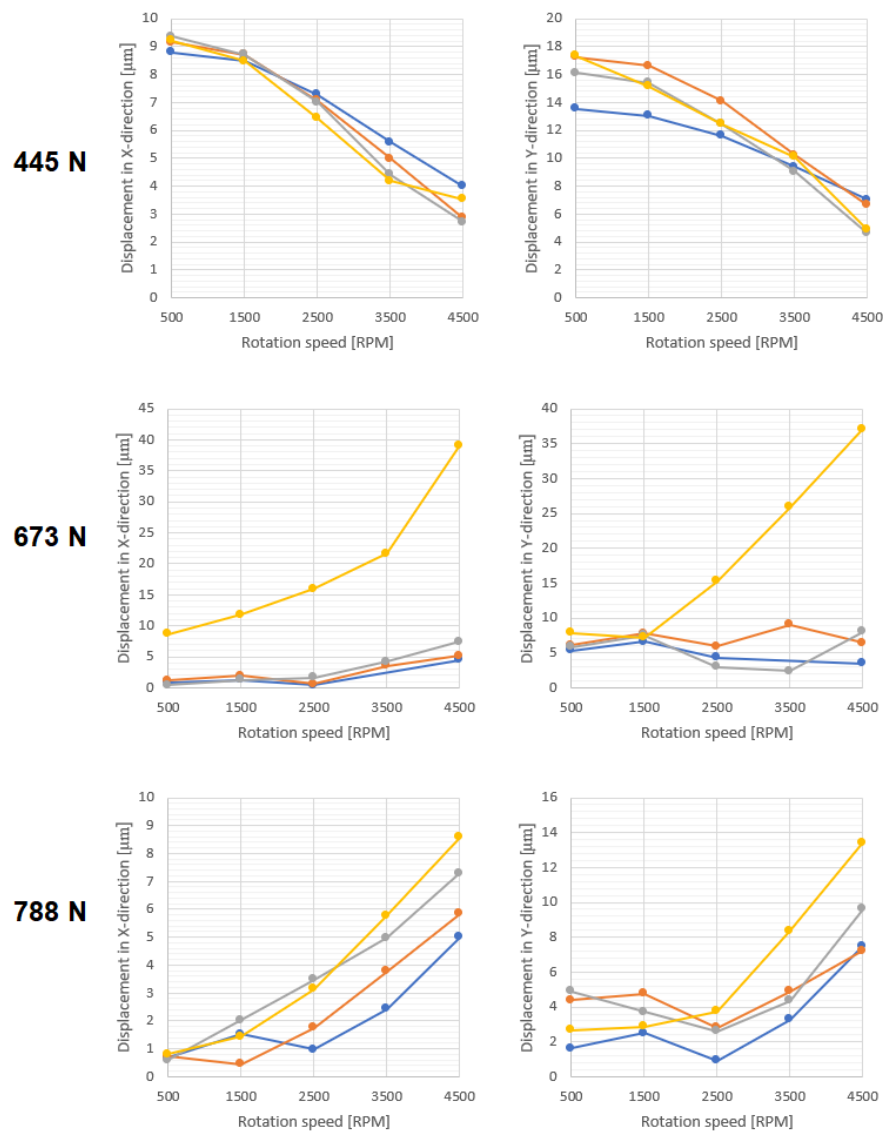


Figure 33. Displacements of DE as a function of rotation speed (blue line represents 14 g unbalance, orange line 22 g unbalance, grey line 30 g unbalance and yellow line 37 g unbalance).

4.3 Estimation of bearing stiffness

From the acquired shaft displacement data, measurement points that are not reliable are excluded from the stiffness estimation. Measurement points with 445 N preload are removed completely due to the phase 180 degree phase difference between the run-out measurement and unbalance measurements, which might be due to a measurement error. Measurement points excluded from 673 N and 788 N preloads are presented in Table 7. Exclusion is done based on the Figures 30 and 33 where cases that do not follow a similar trend are excluded. In the case of DE-measurement with 673 N preload in y -direction (Figure 33) there are no clear visible trend with any of the 14 g to 30 g measurements. Those are still included in the stiffness estimation to present the result for stiffness in y -direction.

Table 7. Excluded measurement points.

Preload [N]	NDE	DE
	Measurement points	Measurement points
673	37 g / 500 RPM	37 g / 500 RPM
	37 g / 1500 RPM	37 g / 1500 RPM
	37 g / 2500 RPM	37 g / 2500 RPM
	37 g / 3500 RPM	37 g / 3500 RPM
	37 g / 4500 RPM	37 g / 4500 RPM
788	14 g / 1500 RPM	14 g / 2500 RPM
	22 g / 1500 RPM	22 g / 1500 RPM
	22 g / 2500 RPM	
	30 g / 2500 RPM	

By excluding the points that do not follow similar trend in Figures 30 and 33 (Table 7), following load-displacement curves are acquired. Figures 34 and 35 present the shaft displacements at NDE with 673 N preload in x - and y -direction, respectively. Figures 36 and 37 present the shaft displacements at NDE with 788 N preload in x - and y -direction, respectively. Figures 38 and 39 present the shaft displacement at DE with 673 N preload in x - and y -direction, respectively and Figures 40 and 41 present the shaft displacements at DE with 788 N preload in x - and y -direction, respectively. Figures 34 to 41 include the stiffness values and correlation coefficients.

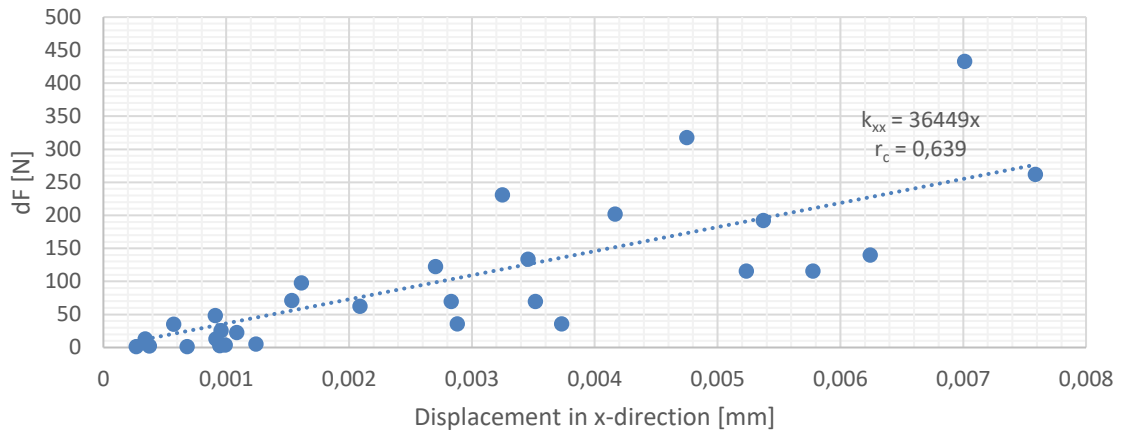


Figure 34. Load-displacement curve of NDE in x -direction with 673 N preload.

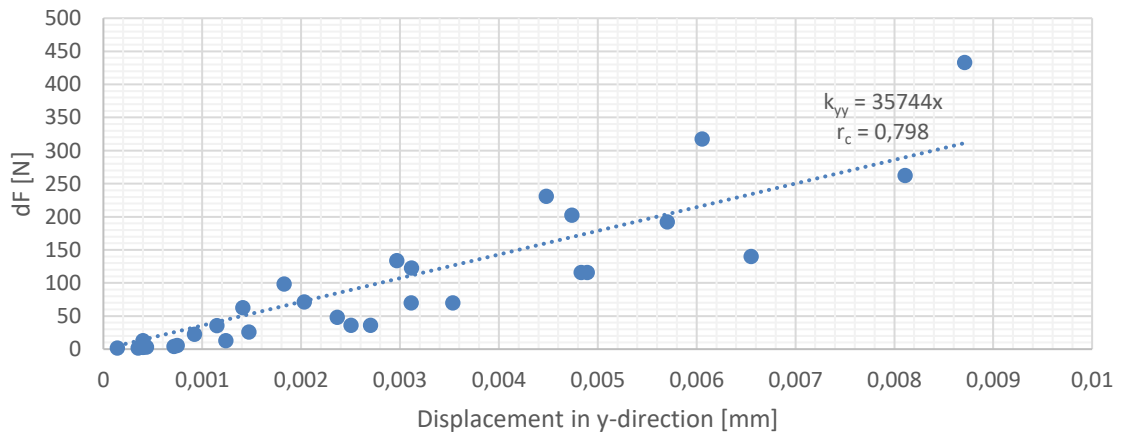


Figure 35. Load-displacement curve of NDE in y -direction with 673 N preload.

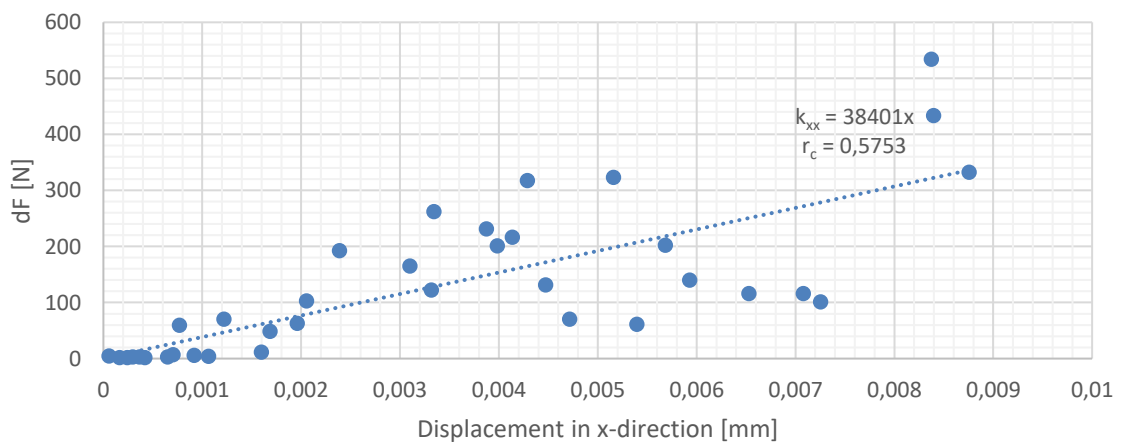


Figure 36. Load-displacement curve of NDE in x -direction with 788 N preload.

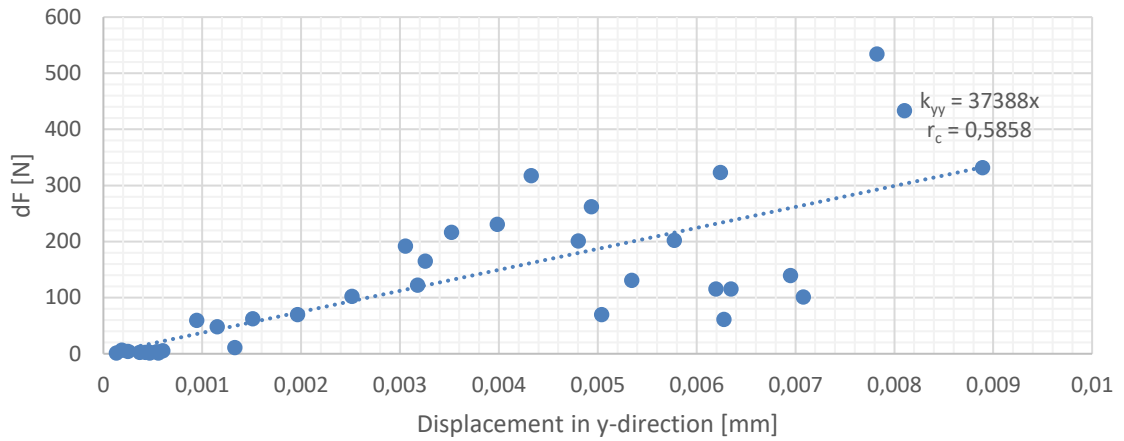


Figure 37. Load-displacement curve of NDE in y -direction with 788 N preload.

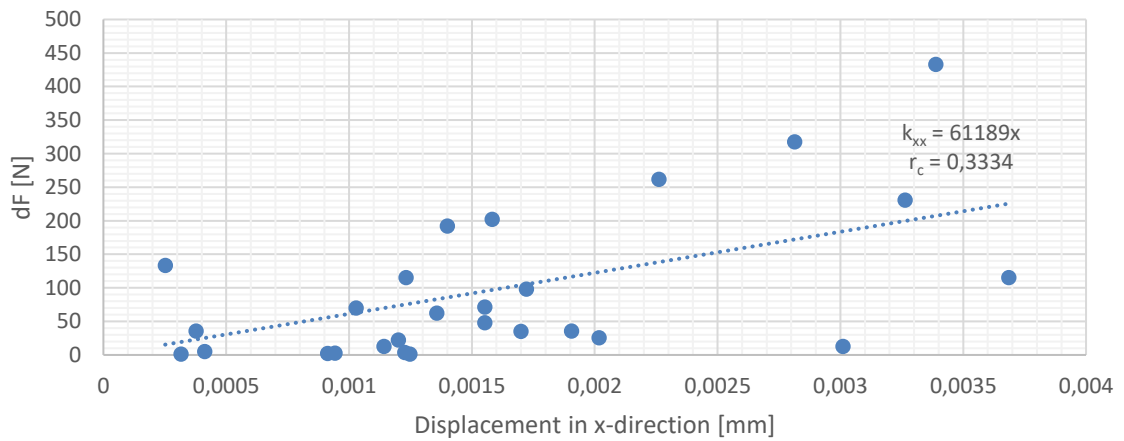


Figure 38. Load-displacement curve of DE in x -direction with 673 N preload.

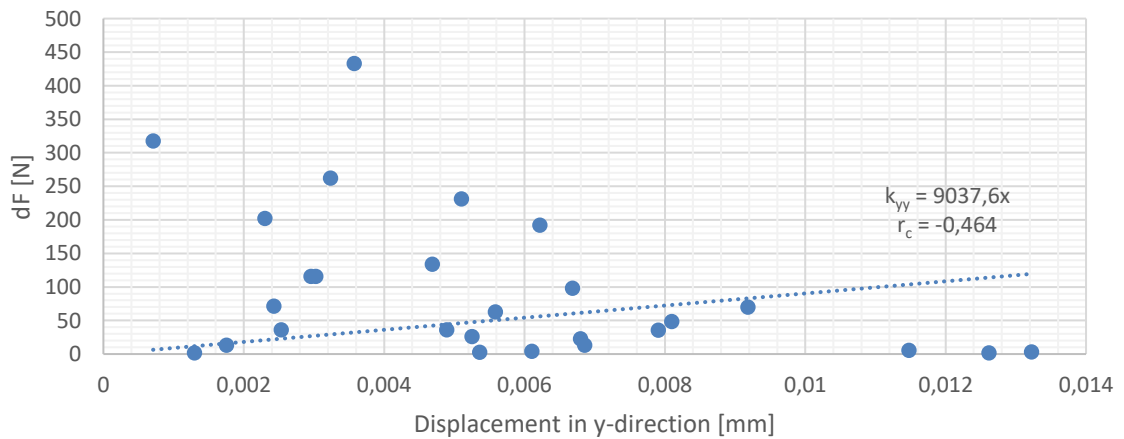


Figure 39. Load-displacement curve of DE in y -direction with 673 N preload.

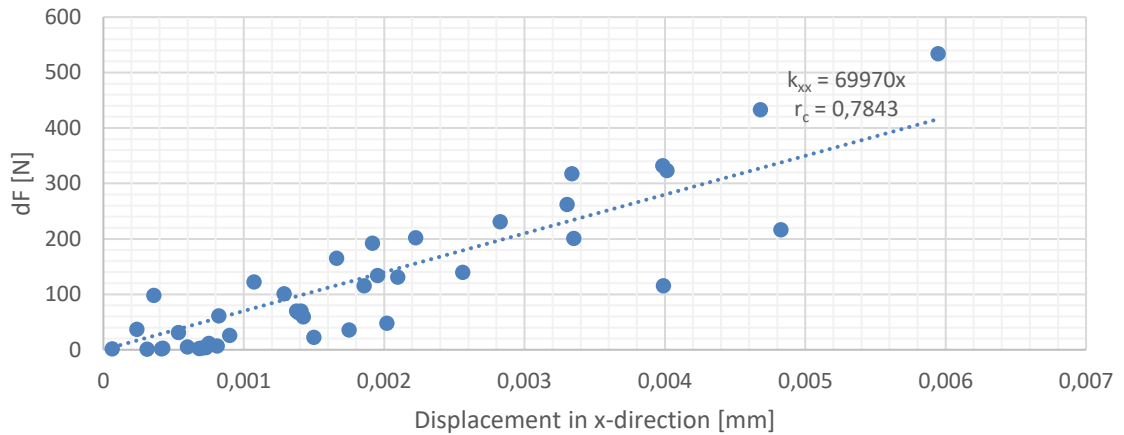


Figure 40. Load-displacement curve of DE in x -direction with 788 N preload.

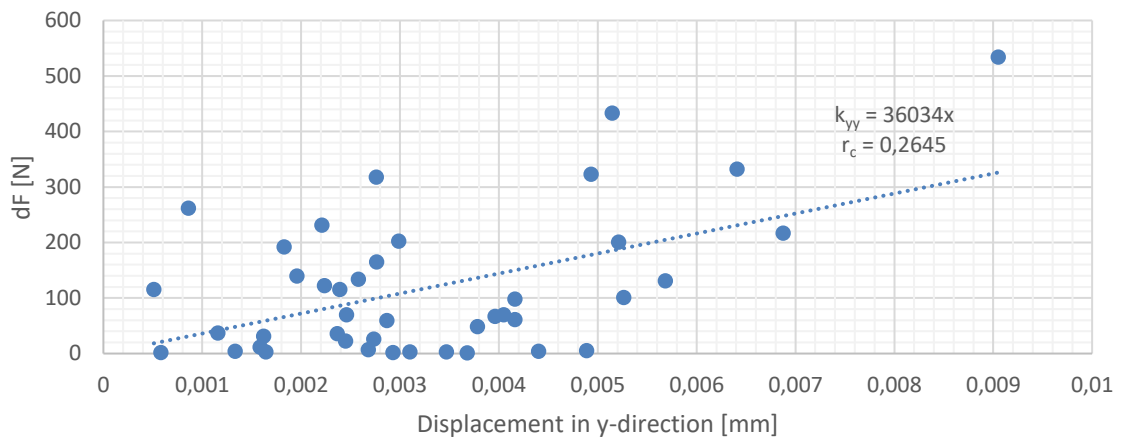


Figure 41. Load-displacement curve of DE in y -direction with 788 N preload.

4.4 Comparison of experimental method to numerical and analytical methods

Table 8 presents the result for stiffnesses in x -direction (k_{xx}) acquired with RoBeDyn and experimentally. Table 9 presents the results for stiffnesses in y -direction (k_{yy}). Tables 10 and 11 presents the results for stiffnesses x -direction (k_{xx}) and in y -direction (k_{yy}), respectively, acquired with BearinX and experimentally. Stiffnesses acquired with Gargiulo's analytical method and experimentally in x -direction (k_{xx}) are presented in Table 12 and in y -direction (k_{yy}) in Table 13. Tables 8 to 12 include the difference between the results in N/mm and also percentage difference, minus sign signifying how much smaller the experimental result is compared to other method and plus sign signifying how much higher the experimental result is compared to other method.

Table 8. Stiffnesses in x-direction, k_{xx} (RoBeDyn compared to experimental).

6209-C-2HRS (NDE-bearing)				
Preload [N]	RoBeDyn [N/mm]	Experimental [N/mm]	Difference [N/mm]	Difference [%]
673	214982	36449	178533	- 83
788	224971	38401	186570	- 83
6309-2Z (DE-bearing)				
Preload [N]	RoBeDyn [N/mm]	Experimental [N/mm]	Difference [N/mm]	Difference [%]
673	235889	61189	174700	- 74
788	247011	69970	177041	- 72

Table 9. Stiffnesses in y-direction, k_{yy} (RoBeDyn compared to experimental).

6209-C-2HRS (NDE-bearing)				
Preload [N]	RoBeDyn [N/mm]	Experimental [N/mm]	Difference [N/mm]	Difference [%]
673	214982	35744	179238	- 83
788	224971	37388	187583	- 83
6309-2Z (DE-bearing)				
Preload [N]	RoBeDyn [N/mm]	Experimental [N/mm]	Difference [N/mm]	Difference [%]
673	235889	9038	226851	- 96
788	247011	36034	210977	- 85

Table 10. Stiffnesses in x-direction, k_{xx} (BearinX compared to experimental).

6209-C-2HRS (NDE-bearing)				
Preload [N]	BearinX [N/mm]	Experimental [N/mm]	Difference [N/mm]	Difference [%]
673	183537	36449	147088	- 80
788	188996	38401	150595	- 80

Table 10 continues. Stiffnesses in x -direction, k_{xx} (BearinX compared to experimental).

6309-2Z (DE-bearing)				
Preload [N]	BearinX [N/mm]	Experimental [N/mm]	Difference [N/mm]	Difference [%]
673	180350	61189	119161	- 66
788	186534	69970	116564	- 62

Table 11. Stiffnesses in y -direction, k_{yy} (BearinX compared to experimental).

6209-C-2HRS (NDE-bearing)				
Preload [N]	BearinX [N/mm]	Experimental [N/mm]	Difference [N/mm]	Difference [%]
673	183537	35744	147793	- 81
788	188996	37388	151608	- 80
6309-2Z (DE-bearing)				
Preload [N]	BearinX [N/mm]	Experimental [N/mm]	Difference [N/mm]	Difference [%]
673	180350	9038	171312	- 95
788	186534	36034	150500	- 81

Table 12. Stiffnesses in x -direction, k_{xx} (Gargiulo compared to experimental).

6209-C-2HRS (NDE-bearing)				
Preload [N]	Gargiulo [N/mm]	Experimental [N/mm]	Difference [N/mm]	Difference [%]
673	61764	36449	25315	- 41
788	61764	38401	23363	- 38
6309-2Z (DE-bearing)				
Preload [N]	Gargiulo [N/mm]	Experimental [N/mm]	Difference [N/mm]	Difference [%]
673	60475	61189	714	+ 1
788	60475	69970	9495	+ 16

Table 13. Stiffnesses in y-direction, k_{yy} (Gargiulo compared to experimental).

6209-C-2HRS (NDE-bearing)				
Preload [N]	Gargiulo [N/mm]	Experimental [N/mm]	Difference [N/mm]	Difference [%]
673	61764	35744	26020	- 42
788	61764	37388	24376	- 39
6309-2Z (DE-bearing)				
Preload [N]	Gargiulo [N/mm]	Experimental [N/mm]	Difference [N/mm]	Difference [%]
673	60475	9038	51437	- 85
788	60475	36034	24441	- 40

5 DISCUSSION

For discussion purposes, x -direction is referred as horizontal direction and y -direction is referred as vertical direction, direction of the axis can be seen in Figure 16. Similarly, 6209-C-2HRS bearing is referred as NDE-bearing and 6309-2Z bearing as DE-bearing.

Stiffnesses acquired experimentally in horizontal direction with 673 N and 788 N preloads range between 36449 N/mm and 38401 N/mm for NDE-bearing and for DE-bearing between 61189 N/mm and 69970 N/mm. In vertical direction the NDE-bearing stiffnesses are between 35744 N/mm and 37388 N/mm while DE-bearing stiffnesses are between 9038 N/mm and 36034 N/mm. Stiffness in vertical direction for DE-bearing with 673 N preload is relatively low when compared to other experimentally acquired results and might be due to a measurement error (Figure 33). NDE-bearing stiffnesses in horizontal and vertical directions are close to each other but for DE-bearing, excluding the 9038 N/mm stiffness measurement, stiffness in vertical direction is 49 % lower than in horizontal direction.

Results for bearing stiffnesses acquired with BearinX- and RoBeDyn-models are higher than experimentally acquired stiffnesses. Experimental results are closer to results acquired with BearinX. Stiffnesses acquired experimentally, excluding the DE-measurement with 673 N preload, are 72 % to 85 % lower than results from RoBeDyn and 62 % to 81 % lower than BearinX-results. Results for DE-bearing are clearly closer to numerically acquired results in horizontal direction, in both RoBeDyn and BearinX. The difference to numerical results in vertical direction are almost the same for both DE- and NDE-bearing. When comparing the experimental results to Gargiulo's analytical method, stiffnesses for NDE-bearing are 38 % to 42 % lower. However, with DE-bearing in horizontal direction, the stiffnesses are higher with the experimental method.

One of the reasons for higher stiffness values in numerical methods is most likely due to the set boundary conditions of the bearings used in the models. Since in the models the outer race of the bearing is fixed the effect of the clearance between the bore of the bearing housing and the bearing outer race is not taken into account. The effect of the clearance is also addressed by Bauer & Werner (2016) (Bauer & Werner 2016, p. 4 – 8). With DE-bearing

the difference in stiffnesses in horizontal direction between numerical and experimental results is smaller than in NDE. This can be due to the smaller clearance between the DE-bearing and the bearing housing. From Table 3 it can be seen that the clearance in NDE is twice the clearance of DE.

Difference between the experimental and numerical methods might also be caused by the axial preload. In experimental measurements, the preload was adjusted by compressing the wave spring with sheet metal shims and preload force was calculated from the spring constant and the deflection of the wave spring. The calculated preload force was then applied to the RoBeDyn- and BearinX-models and kept constant. However, the actual preload used in the system might have been different than those used in numerical models. This can be caused for example, a different spring constant which can be due to manufacturing errors of the wave spring or an installation error in which the preload force is non-uniform on the outer race of the bearing. Additionally, during the experiments the preload might not have been constant due to temperature variations, which can be seen to vary for the bearings in Tables 5 and 6.

By increasing the bearing preload from 673 N to 788 N, NDE-bearing stiffness increases 4,6 % in RoBeDyn and 3 % in BearinX. For the DE, bearing stiffness increases 4,7 % in Robodyn and 3,4 % in BearinX. With the experimental measurements NDE stiffnesses increase 5,4 % in horizontal direction and 4,6 % in vertical direction. Stiffnesses of DE-bearing increase 14,4 % in horizontal direction. Also, there can be seen that preload slightly decreases the difference between the numerical and experimental results.

When comparing the experimental results to Gargiulo's analytical method which takes only in account the geometrical parameters of the bearing, preload or material properties are thus not included, the difference is smaller than in numerical methods. For the DE-bearing in horizontal direction the stiffnesses are actually higher than with Gargiulo's method.

Comparing the results to previous study by Baur & Werner (2016) with bearing stiffness in horizontal direction being 46 % lower than the numerically acquired stiffness in a 650 kW induction motor (Bauer & Werner 2016, p. 1 – 9). When compared to numerical methods, closest result is acquired with BearinX in horizontal direction with 788 N preload, where the

experimental result is 62 % lower. However, in the study there are no information about the clearances between the bearing outer race and the bearing housing or the used software to acquire the numerical result. Additionally, the used bearings are larger than the ones used in this study, at DE the used bearing is 6224 and at NDE 6220 (Bauer & Werner 2016, p. 6.) Outer race diameter for 6224 is 215 mm and 180 mm for 6220 (Schaeffler 2019b; Schaeffler 2019c).

Difference between RoBeDyn and BearinX results can be caused by the material parameters. Since the material properties were not measured those values had to be approximated while in BearinX-software the material properties are from the database. Other reasons may be due to the boundary conditions of the bearing.

5.1 Error sources

Error sources related to experimental measurements include incorrect determination of the phase of the displacement which may be due to a measurements error. These points include the 445 N preload cases where there is 180 degree phase difference between the run-out measurement and unbalance measurements in both DE and NDE. By assuming a measurement error and correcting the phase of x -displacement and y -displacements of run-out measurement, by taking the median value of phases from measurements with added unbalance with 445 N preload. For DE the corrected phase of x -displacement is 164 degrees and for NDE 36 degrees. Corrected phase of y -displacement for DE is 250 degrees and for NDE 282 degrees. Stiffnesses acquired with corrected phase in x -direction for DE-bearing is 74671 N/mm and for NDE-bearing 27642 N/mm. Stiffnesses in y -direction with corrected phase for DE-bearing is 37895 N/mm and 16305 N/mm for NDE-bearing.

Certain measurement points may also been influenced by a resonance of the structure. The vibrations of the DE-shield in horizontal direction during run-up measurement from 0 to 4500 RPM can be used to determine critical speeds. Figure 42 presents the root mean square (RMS) values of acceleration as a function of rotation speed with 14 g unbalance. Figure includes measurements with two preloads 673 N and 788 N, where in the latter the steel frame was mounted on the steel bed from three points. From the figure it can be seen that there are two clear peaks at 2870 and 3990 RPM speeds. These speeds are fairly close to the measurement points of 2500, 3500 and 4500 RPM.

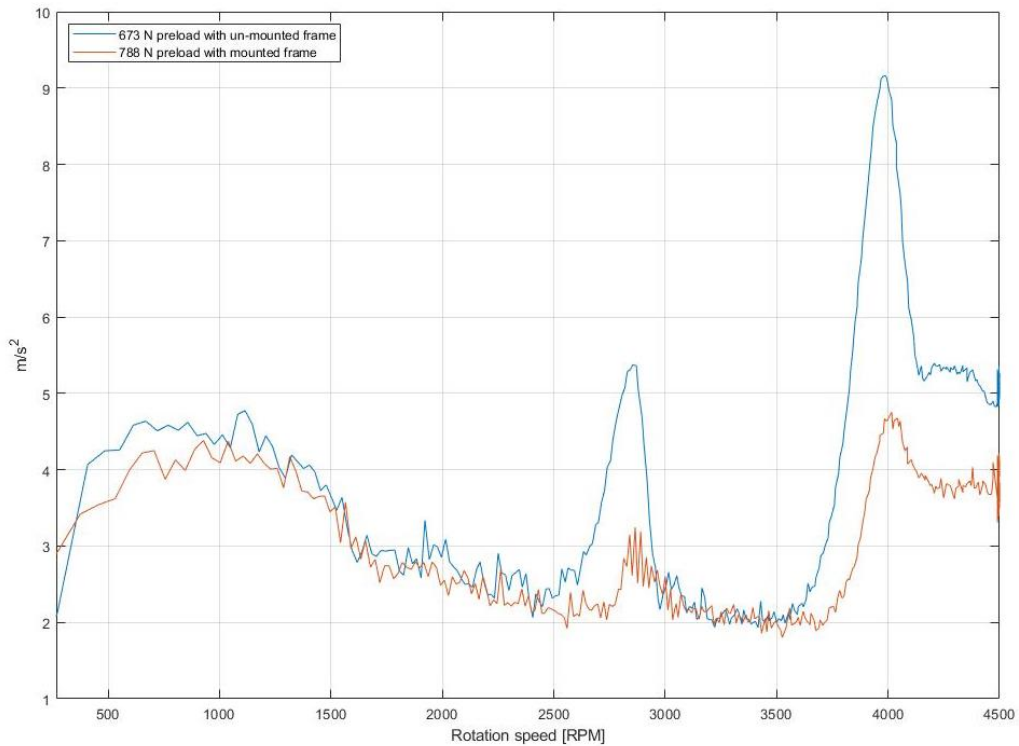


Figure 42. RMS from accelerometer data during 0 – 4500 RPM run up measurement with and without mounted frame.

5.2 Future research

Regarding to the stiffness estimation, results acquired with the proposed method could be compared to other experimental methods, such as method described by Bauer & Werner (2016) to study whether the results are similar. In the future the stiffness estimation could be done for other rolling-element bearings and for large sized electric motors.

For the future research related to the same test rig, some of the measurements conducted in this thesis should be remeasured. These measurements should be done for the measurement points that include a great change in the amplitude or the phase and research if those are due to a measurement error or is those caused by some physical phenomena. Related to the same test rig, the mounting of the frame of the motor to the ground and mounting of the capacitive sensors to the motor frame should be inspected to ensure that there are no excess movement that could interfere with the measurements. Measurement points should also be chosen more carefully to avoid measurement points near the critical speeds of the system that could affect to the results. To avoid measurement error in the determination of the phase, the incremental

encoder could be replaced with an absolute encoder. Additionally, in the current setup the capacitive sensors were not able to measure the displacement from both ends simultaneously.

Also, to increase the FFT resolution the measurement time of capacitive sensors should be increased and acceleration data from both of the housings should be measured. Initially in this thesis, the accelerometer data was acquired from six accelerometers in x -, y -, z -directions from DE and NDE bearing housings, however due to the measurement time only the acceleration in x -direction from DE were measured. For the computational models, more accurate description of the mounting of the outer race of the bearing is required, which in this thesis were mounted to ground.

6 CONCLUSIONS

In this thesis, estimation of the stiffness of rolling-element bearings from the shaft displacement data is studied. Literature review was conducted to get an insight of the multiple parameters affecting to the bearing stiffness that makes the estimation challenging. Literature review also presented the current state of the stiffness estimation categorized as analytical, numerical and experimental methods. As a result of this thesis, a new experimental method to estimate the radial stiffnesses of a rolling-element bearing utilizing a capacitive displacement sensor is proposed.

In this thesis, the radial stiffnesses of DGGBs used in a 11 kW 3-phase induction motor were estimated experimentally with a different static unbalance cases of the shaft and with three different axial preloads of the bearing. Radial stiffnesses were estimated from the relative radial displacement of the shaft caused by the rotating unbalance. With the proposed method, a rotary encoder is required besides the capacitive sensors. Experimentally acquired stiffnesses were then compared to analytically and numerically acquired stiffnesses.

Results indicate that a capacitive sensor can be used to estimate the bearing stiffness, when the system includes a rotary encoder for determination of the phase of the vibration. However, the accuracy of the proposed method should be verified with other experimental methods. Acquired experimental stiffnesses were 62 % to 85 % lower than with numerical methods. When comparing to numerical methods, the experimentally acquired stiffnesses were closer to results calculated by BearinX-software. Stiffnesses acquired with numerically were higher, assumed to be due to set boundary conditions in computational models. When compared to analytical method, the difference to experimentally acquired stiffnesses are smaller than in numerical methods. However, the analytical method is only for a rough estimate.

Possible error sources in the experimental method are discussed and it is clear that more work is required for a more carefully planned measurement procedure. For the current setup, a proper mounting of the motor is required and use of an absolute encoder rather than incremental encoder would be beneficial to limit the possible error sources. Possible error

sources included the effect of the critical speeds to the measurements. Thus, a speed range of measurements should be selected carefully. Results from this thesis can be used to improve the proposed method to possibly improve the accuracy of the results.

7 REFERENCES

ABB. 2014. NEMA Super-E[®] premium efficient motors [web document]. [Referred 4.6.2019]. Available at:

https://library.e.abb.com/public/e35d57ce4df3160285257d6d00720f51/9AKK106369_SuperE_1014_WEB.pdf

ABB. 2015. Motors don't just fail ... do they? – A guide to prevent failure [web document].

Published 2015 [Referred 20.11.2018]. Available at:

https://new.abb.com/docs/librariesprovider53/about-downloads/motors_ebook.pdf?sfvrsn=4

Ali, N.J. & García, J.M. 2010. Experimental studies on the dynamic characteristics of rolling element bearing. Proceedings of the Institution of Mechanical Engineers, Part J: Journal of Engineering Tribology, Vol. 224, Pp. 659 – 666.

Bauer, C. & Werner, U. 2016. Method to detect the critical bending speed of an induction motor by using static rotor eccentricity for deriving the roller bearing stiffness. 11th International Conference on Vibrations in Rotating Machinery, Pp. 1 – 9.

Knaapen, R.J.W. 1997. Experimental determination of rolling element bearing stiffness. Graduation report, p. 1–75.

Dyrobex. 2017. Rolling-Element Bearings [web document]. [Accessed: 28.2.2019]. Available at: <https://dyrobex.com/help1800/Rotor/html/dyro17qs.htm>

El-Sayed, H.R. 1980. Stiffness of Deep-Groove Ball Bearings. Wear, Vol. 63, Iss. 1, pp. 89 – 94.

Gargiulo Jr., E. P. 1980. A Simple Way to Estimate Bearing Stiffness. Machine Design, Vol. 52, Iss. 17, pp. 107 – 110.

Guo, Y. & Parker, R.G. 2012. Stiffness matrix calculation of rolling element bearings using a finite element/contact mechanism model. *Mechanism and Machine Theory*, Vol. 51, pp. 32 – 45.

Hamrock, B. J. & Anderson, W.J. 1983. *Rolling-Element Bearings*. NASA-RP-1105, p. 1–57.

Herbert, W. 2011. *Rolling Element Bearing Basics in Large Electric Motors*. IEEE/IAS Pulp & Paper Industry Technical Paper Conference. Nashville, Tennessee, USA. 19-23.6.2011. P. 189–195.

Houpert, L. 1997. A Uniform Analytical Approach for Ball and Roller Bearing Calculations. *Journal of Tribology*, Vol. 119, pp. 851–858.

Ishida, Y. & Yamamoto, T. 2012. Introduction. In: Ishida, Y. & Yamamoto, T. *Linear and Nonlinear Rotordynamics: A Modern Treatment with Applications*. 2nd edition. Weinheim, Germany. Wiley-VCH Verlag & Co. 2012. Pp. 1–10.

Jacobs, W., Boonen, R., Sas, P. & Moens, D. 2014. Estimating Rolling Element Bearing Stiffness Under Different Operational Condition Through Modal Analysis. In: Dalpiaz, G., Rubini, R., D’Elia, G., Cocconcelli, M., Chaari, F., Zimroz, R., Bartelmus, W. & Haddar, M. *Advances in Condition Monitoring of Machinery in Non-Stationary Operations: Proceedings of the third International Conference on Condition Monitoring of Machinery in Non-Stationary Operations CMMNO 2013, held at Ferrara, Italy*. Springer-Verlag Berlin Heidelberg, 2014. Pp. 103–113.

Kraus, J., Blech, J.J. & Braun, S.G. 1987. In Situ Determination of Rolling Bearing Stiffness and Damping by Modal Analysis. *Journal of Vibration, Acoustics, Stress, and Reliability in Design*, Vol. 109, Iss. 3, pp. 235–240.

Kurvinen, E., Sopanen, J. & Mikkola, A. 2015. Ball Bearing Model Performance on Various Sized Rotors with and without Centrifugal and Gyroscopic Forces. *Mechanism and Machine Theory*, Vol. 90, p. 240 – 260.

Lim, T.C. & Singh, R. 1990. Vibration Transmission Through Rolling Element Bearings, Part I: Bearing stiffness formulation. *Journal of Sound and Vibration*, Vol. 139, Iss. 2, p. 179–199.

PCB Piezotronics. 2019. Model: 622B01 [www- data sheet]. [Referred 22.5.2019]. Available at: <http://www.pcb.com/Products.aspx?m=622B01>

Oswald, F.B., Zaretsky, E.V. & Poplawski, J.V. 2012. Effect of Internal Clearance on Load Distribution and Life of Radially Loaded Ball and Roller Bearings. NASA/TM–2012-217115, p. 1–33.

OVAKO. 2019. 100Cr6 [www- data sheet]. [Referred 31.5.2019]. Available at: <https://steelnavigator.ovako.com/steel-grades/100cr6/>

Pelli, I. 2018. Capacitive Displacement Sensor's Applicability and limitations in Condition Monitoring Systems of Rotating Electrical Machines. Master's Thesis, p. 1–73.

Ragulskis, K.M., Jurkauskas, A.Y., Atstupenas, V.V., Vitkute, A.Y. & Kulvec, A.P. 1974. Determination of Elastic and Damping Characteristics of Rolling-Contact Bearings. In: *Vibration of Bearings*. New Delhi, India. Amerind Publishing Co. Pvt. Ltd. 1979. Pp. 44–88.

Schaeffler. 2015. Materials for Rolling Bearing Technology [web document]. Published 2015 [Referred 28.5.2019]. Available at: https://www.schaeffler.com/remotemedien/media/_shared_media/08_media_library/01_publications/schaeffler_2/tpi/downloads_8/tpi_226_de_en.pdf

Schaeffler. 2019a. Deep groove ball bearings 6209-C-2HRS (Series 62..-C-2HRS) [www- data sheet]. [Referred 23.5.2019]. Available at: https://medias.schaeffler.com/medias/en!hp.ec.br.dp/62..-C-2HRS*6209-C-2HRS

Schaeffler. 2019b. Deep groove ball bearings 6220 (Series 62) [www- data sheet]. [Referred 5.6.2019]. Available at: https://medias.schaeffler.com/medias/en!hp.ec.br.dp/62*6220

Schaeffler. 2019c. Deep groove ball bearings 6224 (Series 62) [www- data sheet]. [Referred 5.6.2019]. Available at: https://medias.schaeffler.com/medias/en!hp.ec.br.dp/62*6224

Schaeffler. 2019d. Deep groove ball bearings 6309-2Z (Series 63..-2Z) [www- data sheet]. [Referred 23.5.2019]. Available at: https://medias.schaeffler.com/medias/en!hp.ec.br.dp/63..-2Z*6309-2Z;bDNQQRJG4nH5

Sheng, X., Li, B., Wu, Z. & Li, H. 2014. Calculation of ball bearing speed-varying stiffness. *Mechanism and Machine Theory*, Vol. 81, pp. 166–180.

Sopanen, J. & Mikkola, A. 2003. Dynamic Model of a Deep Groove Ball Bearing Including Localized and Distributed Defects, Part 1: Theory. *Proceedings of the Institution of Mechanical Engineers K, Journal of Multi-body Dynamics*, Vol. 217, p. 201–211.

Sopanen, J., Kärkkäinen, A., Ghalamchi, B., Heikkinen, J., Kurvinen, E., Halminen, O., Sikanen, E., Hurskainen, V-V., Rahikainen, J., Neisi, N., Kim, H., Choudhury, T. & Jaiswal S. 2019. *RoBeDyn v.2.2 Theory Manual*, p. 1–55.

Stone, B.J. 1982. The State of the Art in Measurement of the Stiffness and Damping of Rolling Element Bearings. *CIRP Annals*, Vol. 31, Iss. 2, pp. 529–538.

Subbiah, R. & Littleton, J.E. 2018. Rotor Balancing: Concept, Modeling and Analysis. In: *Rotor and Structural Dynamics of Turbomachinery: A Practical Guide for Engineers and Scientists*. Springer International Publishing AG. 2018. Pp. 147–196. *Applied Condition Monitoring*, Vol. 11.

Tiwari, M., Gupta, K. & Prakash, O. 2002. Experimental Study of a Rotor Supported by Deep Groove Ball Bearing. *International Journal of Rotating Machinery*, Vol. 8, Iss. 4, p. 243–258.

Tiwari, R. & Vyas, N.S. 1995. Estimation of non-linear stiffness parameters of rolling element bearings from random response of rotor-bearing systems. *Journal of Sound and Vibration*, Vol. 187, Iss. 2, pp. 229–239.

Waide, P. & Brunner, C.U. 2011. Energy-Efficiency Policy Opportunities for Electric Motor-Driven Systems. IEA Energy Papers, p. 1 – 128.

Xiaohu, L., Huanfeng, L., Yanfei, Z. & Jun, H. 2016. Investigation of non-uniform preload on the static and rotational performances for spindle bearing system. International Journal of Machine Tools & Manufacture, Vol. 106, p. 11–21.

Zaretsky, E. V. 2016. Rolling Bearing Life Prediction, Theory, and Application. NASA/TP–2013-215305, p. 1–57.

Table I.1. FAG 6209-C-2HRS and 6309-2Z bearing dimensions.

Dimensions	6209-C-2HRS [mm]	6309-2Z [mm]
Bearing width, B	18,9890	24,9606
Outer diameter of the inner race, d_1	55,8429	61,9796
Inner diameter of the inner race, d	44,99969	44,9917
Outer diameter of outer race, D	84,9981	99,9933
Inner diameter of outer race, D_2	72,6706	83,2749
Inner raceway radius, R_{in}	26,1703	27,5708
Outer raceway radius, R_{out}	38,0862	45,04336
Inner groove radius, r_{in}	6,1372	8,9020
Outer groove radius, r_{out}	6,4983	9,3489
Radial clearance, c_{dy}	0,028	0,030
Axial clearance, c_{dx}	0,158	0,138
Number of balls, Z	10	8
Ball diameter, D_b #1	11,9033	17,4581
Ball diameter, D_b #2	11,9033	17,4581
Ball diameter, D_b #3	11,9033	17,4583
Ball diameter, D_b #4	11,9033	17,4582
Ball diameter, D_b #5	11,9033	-
Average Ball Diameter, D_b	11,9033	17,4582

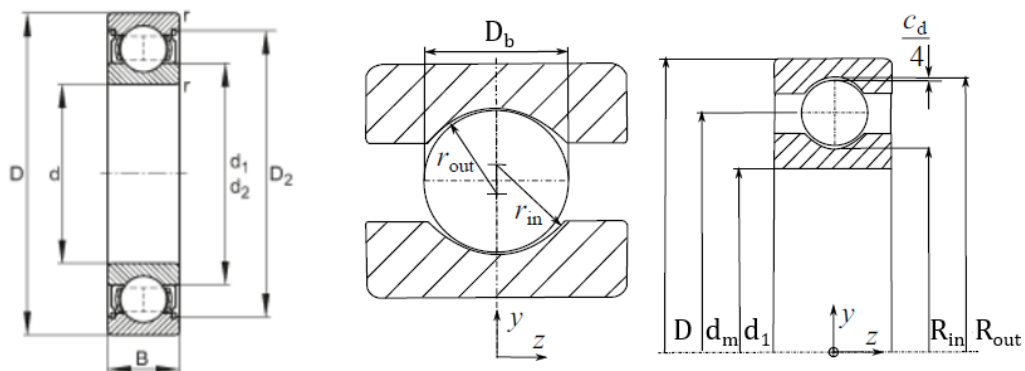


Figure I.1. DGBB dimensions (Schaeffler 2019d; Mod. Kurvinen et al. 2015, p. 244).

Table I.2. Surface roughnesses of bearing shield bores.

	DE-shield	NDE-shield
Ra [μm]	0,8	0,83
Rz [μm]	5,0	9,9
Rmax [μm]	5,2	10,8

Table II.1. Rotor frequencies in x - and y -directions.

Natural frequency	x -direction	y -direction	Difference between x and y
1st bending mode [Hz]	595,3	595,3	0
2nd bending mode [Hz]	1453,9	1446,9	7
3rd bending mode [Hz]	2099,2	2085,2	14

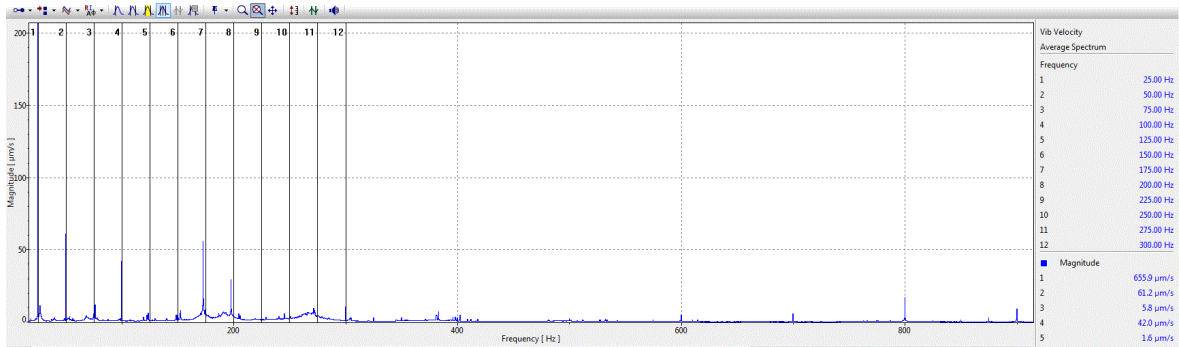
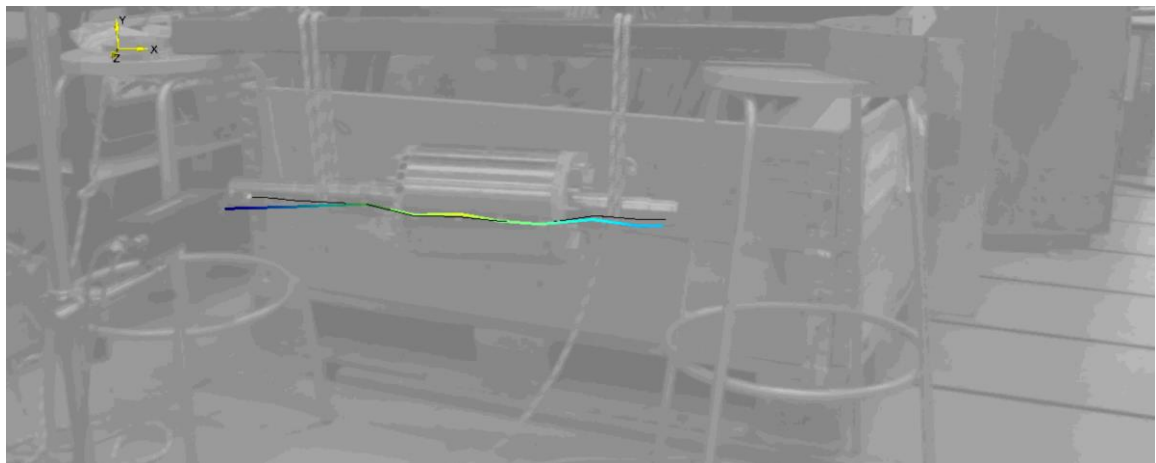


Figure II.1. FFT of motor operating at 1500 RPM with no load.

Figure II.2. 1st bending mode in x -plane at 595 Hz.

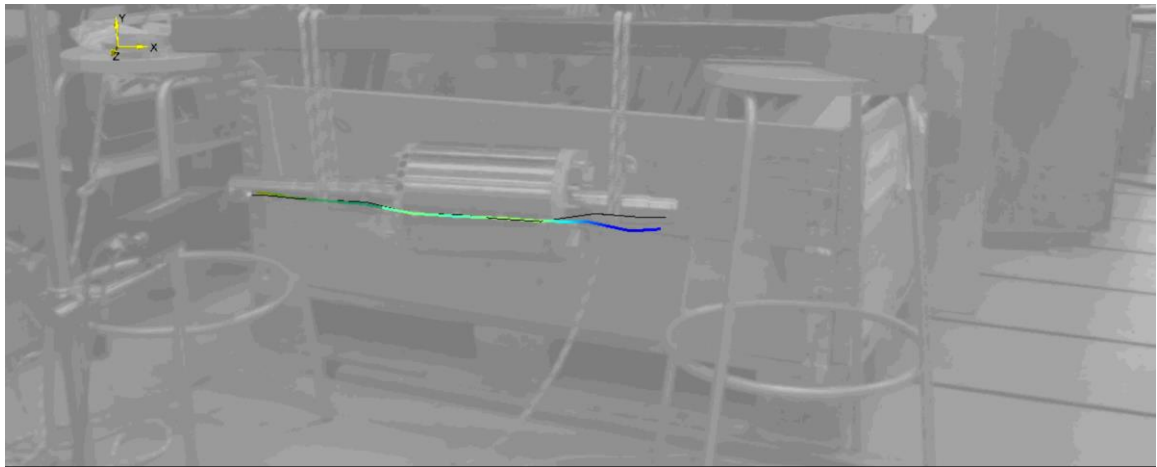


Figure II.3. 2nd bending mode in x-plane at 1459 Hz.

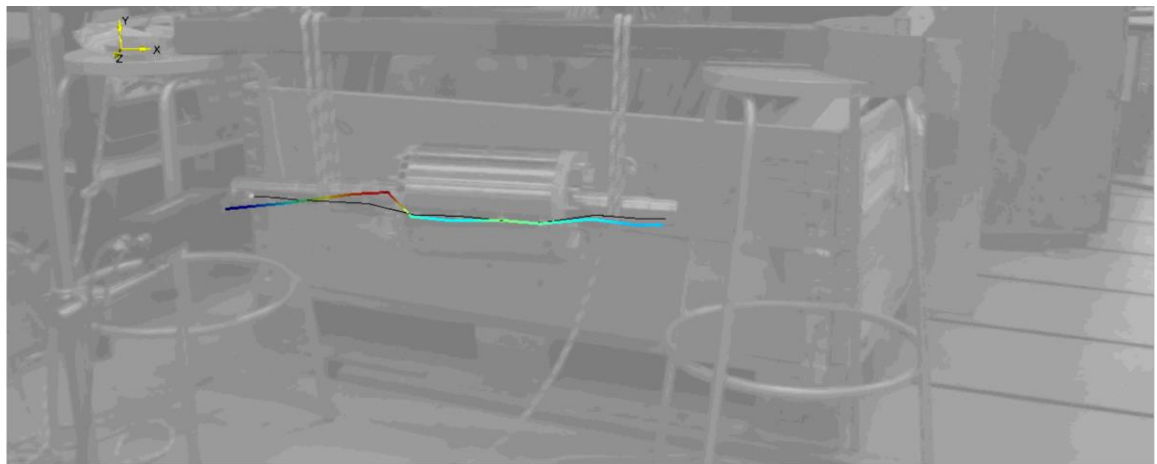


Figure II.4. 3rd bending mode in x-plane at 2099 Hz.

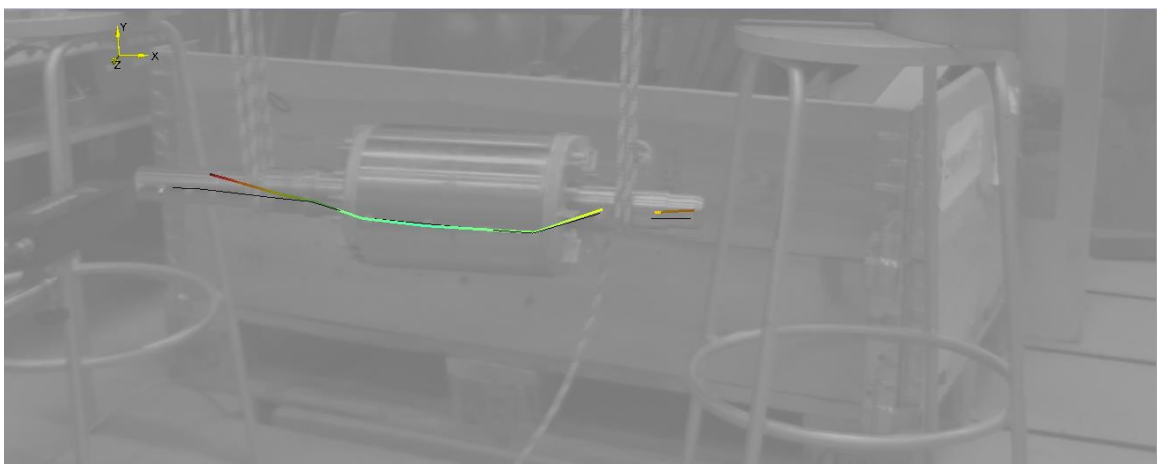


Figure II.5. 1st bending mode in y-plane at 595 Hz.

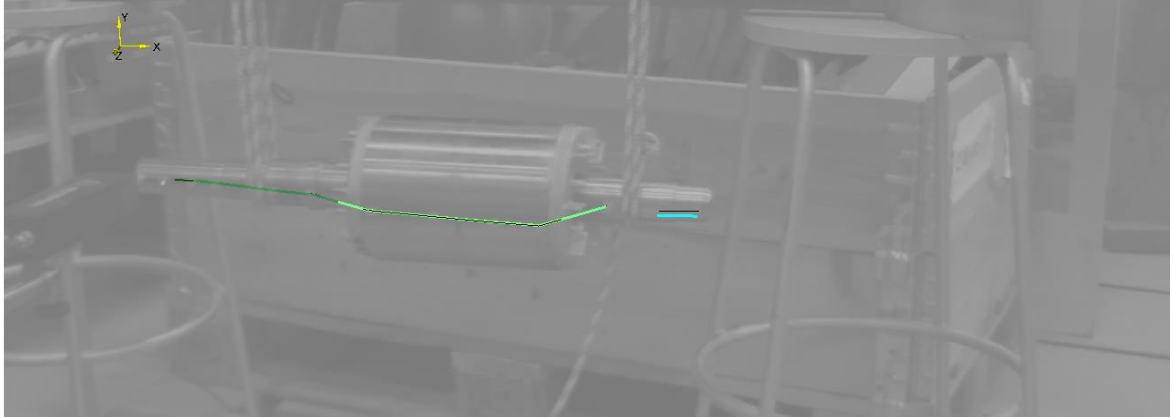


Figure II.6. 2nd bending mode in y-plane at 1446 Hz.

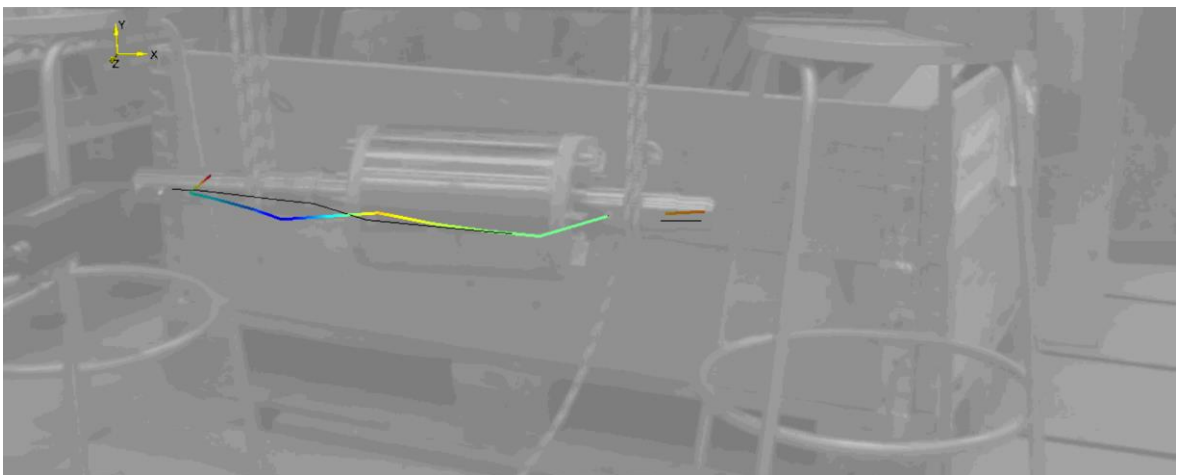
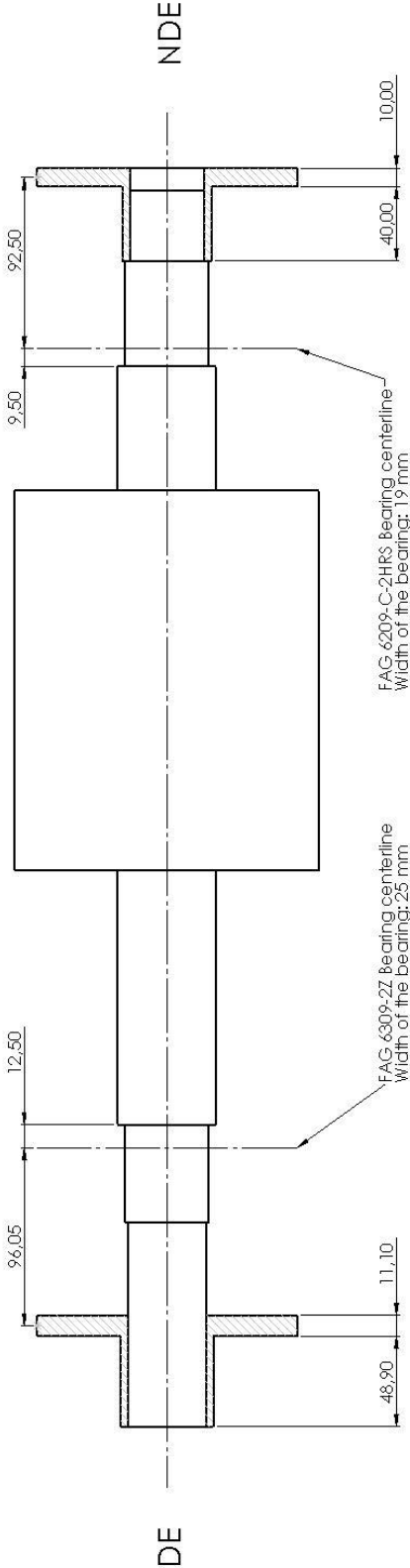


Figure II.7. 3rd bending mode in y-plane at 2085 Hz.



Figure II.8. ODS measurement at 1500 RPM with no load.



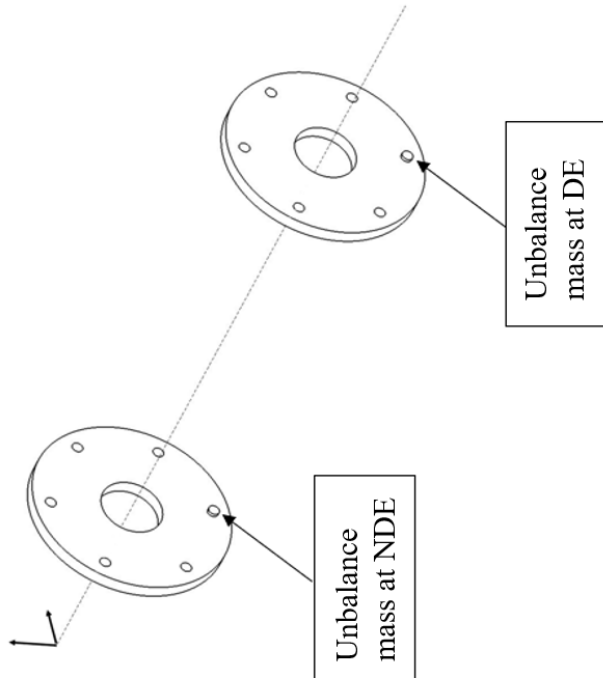
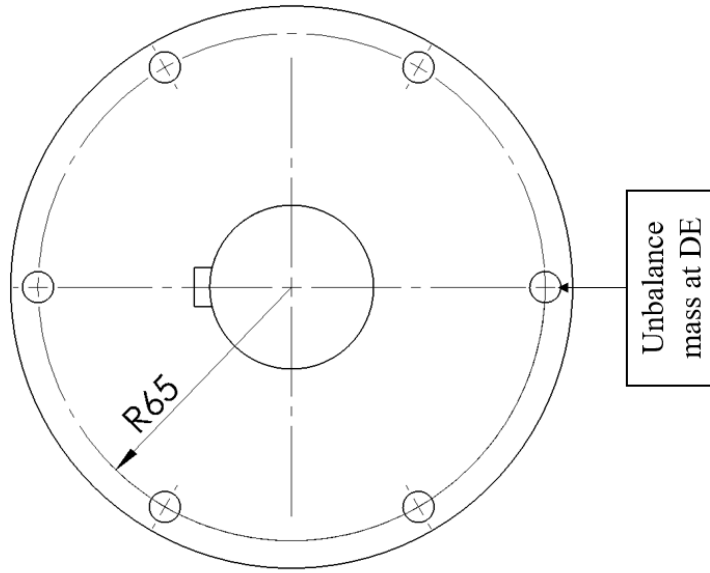


Table IV.1. Shaft displacement measurements at NDE, 445 N preload.

X-direction					
UB	Rotation Speed [RPM]				
[g]	500	1500	2500	3500	4500
0	2,65∠208,30°	2,67∠193,36°	3,13∠180,35°	2,91∠217,97°	2,54∠158,73°
14	3,16∠34,10°	3,10∠17,23°	4,19∠29,88°	3,68∠27,77°	5,70∠337,85°
22	3,22∠37,44°	3,27∠37,27°	4,26∠24,96°	3,98∠349,10°	7,53∠9,14°
30	3,18∠43,77°	3,54∠31,64°	5,07∠12,66°	5,13∠317,81°	10,77∠290,39°
37	3,21∠44,12°	3,37∠31,29°	5,93∠337,50°	5,52∠9,49°	14,57∠299,00°
Y-direction					
UB	Rotation Speed [RPM]				
[g]	500	1500	2500	3500	4500
0	2,56∠110,21°	2,58∠96,15°	2,90∠84,73°	2,73∠119,18°	2,20∠61,00°
14	3,06∠296,02°	2,84∠279,84°	3,89∠291,80°	3,83∠285,12°	6,00∠241,88°
22	3,15∠295,31°	3,12∠294,61°	4,29∠284,77°	4,33∠244,69°	8,40∠274,22°
30	3,15∠305,33°	2,92∠294,61°	4,74∠271,58°	5,93∠216,21°	12,63∠204,26°
37	3,26∠304,63°	2,94∠293,20°	5,64∠235,20°	6,95∠268,24°	16,17∠217,62°

Table IV.2. Shaft displacement measurements at NDE, 673 N preload.

X-direction					
UB	Rotation Speed [RPM]				
[g]	500	1500	2500	3500	4500
0	2,7∠333,5°	3,2∠351,9°	3,5∠331,9°	3,5∠32°	3,4∠325,2°
14	2,9∠340°	3,4∠333,3°	4,5∠358,6°	5,1∠2,1°	6,6∠292,5°
22	2,9∠353,5°	3,7∠347,3°	5∠323,8°	5,6∠324,1°	8,1∠332,6°
30	2,9∠358,8°	4,0∠344,9°	6,0∠2,1°	6,52∠298,5°	9,8∠296,5°
37	2∠101,1°	2∠107,1°	1,7∠134,6°	0,8∠340,7°	1,4∠260,9°
Y-direction					
UB	Rotation Speed [RPM]				
[g]	500	1500	2500	3500	4500

APPENDIX IV, 2

Table IV.2. continues. Shaft displacement measurements at NDE, 673 N preload.

0	2,1∠244,7°	2,4∠264,4°	2,5∠244°	2,3∠302,7°	1,7∠250,7°
14	2,5∠244°	2,7∠244,7°	3,5∠263,3°	4,5∠262,6°	5,6∠199°
22	2,8∠247,9°	3,1∠245,2°	4∠225°	5,7∠224,3°	7,7∠237,7°
30	2,8∠250,8°	3,9∠229,6°	5,4∠253,8°	7,3∠200,4°	9,9∠208,7°
37	2,6∠182°	2,5∠181,6°	0,8∠219°	1∠174°	3,5∠7,7°

Table IV.3. Shaft displacement measurements at NDE, 788 N preload.

X-direction					
UB	Rotation Speed [RPM]				
[g]	500	1500	2500	3500	4500
0	3,04∠69,43°	3,26∠68,91°	3,06∠65,74°	3,48∠55,90°	3,99∠79,80°
14	3,13∠81,39°	3,5∠70,31°	3,63∠98,44°	4,75∠100,2°	6,53∠20,04°
22	3,34∠87,89°	3,70∠74,18°	3,96∠75,94°	5,79∠48,16°	8,19∠71,19°
30	3,34∠85,08°	3,70∠95,98°	4,20∠74,88°	6,52∠39,02°	10,24∠27,77°
37	3,16∠82,27°	4,00∠72,42°	5,59∠90,70°	8,12∠80,51°	12,15∠64,34°
Y-direction					
UB	Rotation Speed [RPM]				
[g]	500	1500	2500	3500	4500
0	2,84∠338,55°	3,10∠338,20°	2,76∠340,14°	3,20∠326,60°	3,62∠349,28°
14	3,14∠344,36°	3,52∠333,28°	3,70∠1,41°	4,97∠5,27°	6,56∠287,93°
22	3,17∠346,64°	3,63∠333,11°	4,06∠336,09°	6,04∠311,84°	7,85∠339,26°
30	3,44∠338,20°	3,99∠349,98°	4,79∠336,09°	7,70∠303,05°	10,07∠301,29°
37	2,99∠340,66°	3,92∠330,64°	5,97∠348,05°	9,18∠345,59°	11,37∠339,26°

Table IV.4. Shaft displacement measurements at DE, 445 N preload.

X-direction					
UB	Rotation Speed [RPM]				
[g]	500	1500	2500	3500	4500
0	4,31∠335,92°	4,23∠347,87°	3,40∠326,95°	2,78∠323,79°	1,42∠327,30°
14	4,47∠158,73°	4,21∠166,64°	2,99∠143,70°	1,26∠147,66°	1,32∠269,21°

APPENDIX IV, 3

Table IV.4. continues. Shaft displacement measurements at DE, 445 N preload.

22	4,85∠148,18°	4,41∠161,37°	2,93∠130,25°	0,71∠177,54°	2,25∠299,18°
30	5,05∠157,15°	4,46∠142,21°	2,73∠166,99°	0,48∠237,66°	3,87∠297,69°
37	4,91∠151,52°	4,19∠147,48°	2,33∠186,68°	1,28∠260,16°	5,33∠204,61°
Y-direction					
UB	Rotation Speed [RPM]				
[g]	500	1500	2500	3500	4500
0	7,41∠63,98°	7,22∠75,59°	6,00∠54,14°	5,10∠48,87°	2,47∠44,30°
14	6,33∠262,44°	6,03∠272,81°	4,21∠252,77°	2,13∠269,30°	3,48∠354,38°
22	9,87∠248,20°	9,43∠263,32°	6,71∠235,20°	3,21∠279,14°	2,51∠1,76°
30	8,72∠250,84°	8,02∠235,72°	5,12∠255,94°	1,65∠236,95°	6,23∠25,49°
37	9,90∠243,11°	7,73∠239,24°	5,41∠271,76°	2,84∠220,78°	2,99∠39,02°

Table IV.5. Shaft displacement measurements at DE, 673 N preload.

X-direction					
UB	Rotation Speed [RPM]				
[g]	500	1500	2500	3500	4500
0	3,96∠95,63°	4,02∠91,41°	2,89∠112,15°	2,53∠127,62°	1,45∠180,00°
14	4,87∠96,68°	5,21∠93,34°	4,09∠101,78°	-	0,55∠274,22°
22	5,18∠97,38°	5,51∠81,56°	4,47∠101,25°	1,83∠160,31°	1,53∠321,68°
30	4,08∠90,00°	4,00∠113,73°	2,84∠117,07°	1,14∠190,90°	3,73∠245,21°
37	7,34∠0,35°	9,23∠333,63°	14,92∠357,89°	20,25∠349,45°	35,45∠252,25°
Y-direction					
UB	Rotation Speed [RPM]				
[g]	500	1500	2500	3500	4500
0	5,62∠186,68°	5,55∠180,00°	4,40∠200,39°	4,00∠216,91°	2,12∠271,41°
14	10,96∠190,20°	12,22∠189,14°	9,89∠191,60°	-	2,76∠217,00°
22	11,58∠196,00°	13,44∠183,52°	11,07∠203,91°	7,36∠274,57°	2,09∠290,74°
30	11,50∠187,73°	12,07∠214,10°	8,51∠179,12°	3,76∠167,70°	2,45∠14,06°
37	8,38∠251,72°	10,74∠224,82°	17,29∠246,45°	28,09∠248,20°	42,49∠10,16°

Table IV.6. Shaft displacement measurements at DE, 788N preload.

X-direction					
UB	Rotation Speed [RPM]				
[g]	500	1500	2500	3500	4500
0	4,14∠183,08°	4,17∠183,34°	2,93∠198,63°	2,59∠209,53°	1,37∠183,52°
14	4,82∠183,69°	4,61∠202,15°	3,19∠186,33°	1,74∠191,60°	0,85∠5,98°
22	4,86∠184,22°	4,59∠182,11°	3,02∠205,31°	0,88∠242,93°	2,30∠54,84°
30	4,60∠188,09°	4,07∠211,64°	2,26∠240,47°	0,85∠351,91°	3,47∠330,12°
37	4,59∠191,95°	4,38∠202,32°	2,68∠232,73°	1,67∠349,45°	4,70∠335,74°
Y-direction					
UB	Rotation Speed [RPM]				
[g]	500	1500	2500	3500	4500
0	6,78∠278,26°	6,69∠279,14°	4,87∠284,06°	4,01∠308,67°	2,35∠291,09°
14	8,42∠278,79°	8,02∠295,31°	5,87∠277,73°	3,50∠274,92°	0,94∠55,90°
22	11,05∠271,05°	11,26∠267,54°	8,94∠291,80°	5,35∠324,14°	0,49∠75,59°
30	11,45∠268,95°	10,45∠286,17°	6,87∠300,23°	3,15∠308,67°	2,84∠96,33°
37	9,27∠285,47°	9,02∠291,45°	5,88∠311,84°	2,06∠52,73°	7,34∠61,70°